Scilight

Applied Mathematics and Statistics
https://www.sciltp.com/journals/ams

Article

Check for updates

Compartmental Description of the Cosmological Baryonic Matter Cycle. Inclusion of Triggered Star Formation

Martin Kröger [1,2,*] and Reinhard Schlickeiser [3,4,*]

[1] Magnetism and Interface Physics, Department of Materials, ETH Zurich, CH-8093 Zurich, Switzerland
[2] Computational Polymer Physics, Department of Materials, ETH Zurich, CH-8093 Zurich, Switzerland
[3] Institut für Theoretische Physik, Lehrstuhl IV: Weltraum- und Astrophysik, Ruhr-Universität Bochum, D-44780 Bochum, Germany
[4] Institut für Theoretische Physik und Astrophysik, Christian-Albrechts-Universität zu Kiel, Leibnizstr. 15, D-24118 Kiel, Germany
* Correspondence: mk@mat.ethz.ch (M.K.); rsch@tp4.rub.de (R.S.)

How To Cite: Kröger, M.; Schlickeiser, R. Compartmental Description of the Cosmological Baryonic Matter Cycle. Inclusion of Triggered Star Formation. *Applied Mathematics and Statistics* **2026**, *3*(1), 6. https://doi.org/10.53941/ams.2026.100006

Received: 1 April 2026
Revised: 24 April 2026
Accepted: 27 April 2026
Published: 6 May 2026

Abstract: *Purpose:* The earlier introduced compartmental description, well-known from the statistical description of infection diseases and epidemics, was adopted here to describe the nonlinear temporal evolution of the baryonic matter compartments in interstellar gas (G) and stars (S) in the presence of triggered star formation. The primary astrophysical goal of our study is the explanation of the cosmological star formation history. The competition of triggered star formation, spontaneous star formation, stellar feedback, and stellar evolution was theoretically investigated to understand the baryonic matter cycle, including luminous baryonic matter in main-sequence stars and weakly luminous matter in white dwarfs, neutron stars and black holes. Of particular interest was the understanding of the cosmic star formation history and the redshift dependence of the gas and stellar fractions using compartmental models. *Methods:* For stationary rates of spontaneous and triggered star formation, continuous stellar feedback and stellar evolution, exact and approximate analytical solutions of the time evolution of the fractions of stellar and locked-in stellar matter were derived involving the time dependence of the gaseous fraction $G(t)$. The high accuracy of the analytical solutions is proven by comparison with the exact numerical solutions of the GSL equations. *Results:* The inclusion of the triggered star formation process explains the observed cosmological star formation rate, the integrated stellar density at redshifts below $z = 8$, and the present-day gas and stellar fractions very well. The generalized GSL-model provides excellent fits to the observed redshift dependencies of the star formation rate and the integrated stellar density. Moreover, it explains the observed present-day gas and stellar fractions, and it makes predictions on the future evolution of these fractions in the universe.

Keywords: galaxy evolution; star formation; stellar matter; nonlinear dynamical system; statistical physics

1. Introduction

Recently [1]—hereafter referred to as part I—the compartmental description, well-known from the statistical description of infection diseases and epidemics [2–26], has been introduced to describe the temporal evolution of the baryonic matter compartments in interstellar gas and stars. Such a statistical description makes use of gaseous and stellar fractions of the total baryonic matter and transition rates between these fractions. In particular, the respective rates of spontaneous ($\beta(t)G(t)$) and triggered ($a(t)S(t)G(t)$) star formation regulate the transfer $G(t) \to S(t)$ from gas to luminous main-sequence stars, whereas the stellar feedback rate ($b(t)S(t)$) determines the feedback $S(t) \to G(t)$ from luminous stars to gas. Thirdly the stellar evolution rate ($c(t)S(t)$) regulates the transfer

$S(t) \to L(t)$ from luminous stars to locked-in stellar matter in the form of white dwarfs, neutron stars and black holes, which are much less luminous and have no significant stellar feedback to the gaseous matter compartment.

There are many similarities between the compartment models describing the dynamics of epidemics and the baryonic matter cycle [27–29]. In epidemiology, one considers individual populations with a large number N of persons, that are either susceptible to infections, are infected or recovered/removed from the infection. Each of these three compartments is characterized by time-dependent fractions $S(t)$, $I(t)$, $R(t)$ obeying the dynamical SIR-equations. Concerning the baryonic matter cycle description these three compartments correspond to the time-dependent fractions of gas $G(t)$, luminous stars $S(t)$ and locked-in stellar matter $L(t)$, respectively, being subject to the dynamical GSL-model whose mathematical form is similar to the epidemic SIR-model, but not identical as it includes additionally the effects of spontaneous star formation and stellar feedback. In epidemiology, one applies the fractions from the compartment models to individual countries or regions by multiplying them by the total number of people N in these regions. Therefore, by no means the SIR epidemic models built only for the population of the whole Earth as one entity. The application of the compartment model to the population in different spatial regions is possible and successful [30], provided only that the number of persons N in this region is high enough that a statistical description with ensemble-averaged infection and recovery rates is justified. Correspondingly, the dynamical GSL-model can also be applied to individual constituents of the Universe, such as groups of galaxies provided the number of luminous baryons is high enough. If one compares with observations of stars summed or averaged over many galaxies, as will be done here, the compartment model is particularly appropriate and justified.

In part I, the process of triggered star formation has been ignored, and the resulting exact analytical solutions for stationary rates of spontaneous formation, feedback and evolution have been compared with the observed cosmological star formation rate and the integrated stellar density. It has been demonstrated that the simplified GS-model ignoring stellar evolution cannot explain the observations. The comparison of the full gas-stars-locked-in (GSL) model, including stellar evolution is more favorable but still far from being perfect. The non-perfect agreement of the GSL-model with only the spontaneous star formation process, therefore is a strong motivation to investigate the role of the additional triggered star formation process, which is the subject of the present investigation.

Here, the competition of triggered and spontaneous star formation, stellar feedback, and stellar evolution is theoretically investigated with analytical and numerical solutions of the nonlinear dynamical GSL equations. Following part I, baryonic matter exists as interstellar and intergalactic gas with the fraction $G(t)$ and in two forms of stellar matter: $S(t)$ denotes the fraction of luminous stellar matter in main-sequence stars while $L(t)$ refers to the fraction of weakly luminous matter in white dwarfs, neutron stars and black holes (referred to as locked-in matter) which have no significant stellar feedback to the gaseous matter compartment. Powerful stellar winds and supernovae cause stellar feedback. The temporal evolution of the three fractions is controlled by the respective rates of spontaneous star formation ($\beta(t)G(t)$) and of triggered star formation ($a(t)G(t)S(t)$ of gas to stellar matter, of stellar feedback ($b(t)S(t)$) of stellar to gaseous matter, and of the formation ($c(t)S(t)$) of white dwarfs, neutron stars and black holes from stellar evolution. Obviously, the inclusion of triggered star formation introduces a nonlinearity in the GSL equations as it depends on the product $G(t)S(t)$. The primary astrophysical goal of our study is the explanation of the cosmological star formation history.

The organization of this manuscript is as follows. The GSL-compartmental model for the baryonic matter cycle is revisited in Section 2. While Section 3 is concerned with the GS-limit for negligible stellar evolution, the full GSL model for stationary ratios is investigated in Section 4. Having obtained general relationships between the compartments, and their limiting, stationary values, approximate solutions are derived and tested in Section 5. Section 6 connects the GSL fractions with the cosmic star formation history and discusses observational constraints that help us identify the parameters of the GSL model. The resulting redshift dependency of the gas and stellar fractions is presented in Section 7. A summary and conclusions are provided in Section 8.

2. GSL-Compartmental Model for the Baryonic Matter Cycle

As in part I we considered the total system of matter either in stars or in interstellar gas and introduce the compartments G (gas), S (stars) and L (locked-in matter in white dwarfs, neutron stars and black holes) where $G(t)$, $S(t)$ and $L(t)$ denote the relative fractions of luminous matter in the three compartments, respectively, as a function of time t.

2.1. Starting Equations

The three fractions obey the sum constraint.

$$G(t) + S(t) + L(t) = 1, \tag{1}$$

holding at all times t after the beginning of the baryonic evolution at time $t = t_0$. The dynamical evolution of the three fractions is described by the nonlinear dynamical GSL equations (Figure 1)

$$\frac{dG}{dt} = -a(t)G(t)S(t) - \beta(t)G(t) + b(t)S(t), \tag{2}$$

$$\frac{dS}{dt} = a(t)G(t)S(t) + \beta(t)G(t) - b(t)S(t) - c(t)S(t), \tag{3}$$

respectively. The sum constraint (1) then implies

$$\frac{dL}{dt} = c(t)S(t); \tag{4}$$

as initial condition in the presence of spontaneous star formation ($\beta(t) > 0$) we adopted

$$G(t_0) = 1, \quad S(t_0) = 0, \quad L(t_0) = 0. \tag{5}$$

The initial time t_0 corresponds to the redshift $z = 1100$ as in part I. As an aside, we note that in the absence of spontaneous star formation ($\beta = 0$) the initial conditions (5) had to be modified to $G(t_0) = 1 - \eta$, $S(t_0) = \eta$, $L(t_0) = 0$, with the small initial stellar fraction $\eta \ll 1$. Without a finite albeit tiny initial fraction, the process of triggered star formation does not start.

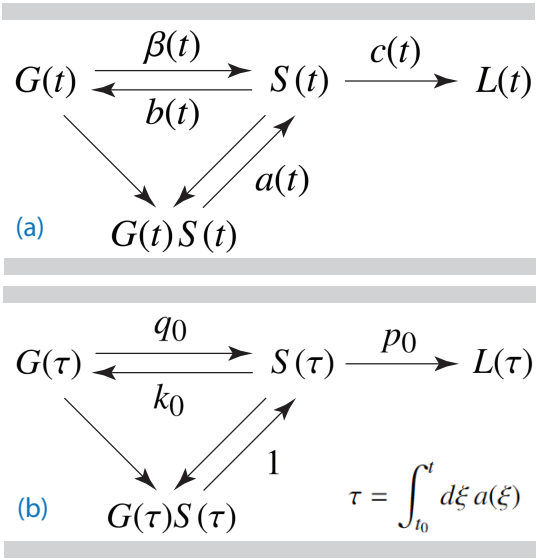

Figure 1. GSL model. (**a**) Schematic diagram for the nonlinear dynamical exchange (2)–(4) between gas (G), star (S), and locked-in (L) baryonic matter fractions, regulated by the four potentially time-dependent rates $a(t)$, $b(t)$, $c(t)$, and $\beta(t)$. (**b**) Equivalent dynamical equations (14) for the fractions in reduced time τ, with the dimensionless, stationary rates k_0, p_0, and q_0. Panel (**a**) reprinted with permission from [1].

As before in part I, we chose with Equations (1)–(5) a "closed box" system description where the total amount of baryonic matter is conserved and contained in at least one of the three fractions. As emphasized before, this description can be applied to large-enough individual systems in the universe. If one opts to generalize the closed-box description accounting for losses or gains of matter, caused e.g., by the ejection of gas out of the galaxy by supernovae and black hole feedback, and the accretion of fresh gas from its host environment atmosphere, respectively (see the review [31]), the dynamical models considered in [32] are more appropriate.

Of particular interest is the formation rate $\mathring{J}(t)$ of new stars as a function of time,

$$\mathring{J}(t) = a(t)G(t)S(t) + \beta(t)G(t), \tag{6}$$

where the first term represents the rate from triggered star formation, while the second term is the rate from spontaneous star formation.

In contrast to part I we also included in the analysis the process of triggered star formation, which is nonlinear as it depends on the product $G(t)S(t)$. Exact and approximate analytical solutions of the dynamical equations of the GSL-model (1)–(5) were derived, which hold for stationary rates as well as for the case of the same time dependency of all rates.

2.2. Stationary Ratios

We here introduced the three ratios.

$$k(t) = \frac{b(t)}{a(t)}, \qquad q(t) = \frac{\beta(t)}{a(t)}, \qquad p(t) = \frac{c(t)}{a(t)}, \tag{7}$$

indicating the strength of stellar feedback, spontaneous star formation, and stellar evolution with respect to triggered star formation, respectively.

For ease of exposition, we considered, similar to part I, the case of stationary ratios $k(\tau) = k_0 = \text{const}$, $q(\tau) = q_0 = \text{const}$, and $p(\tau) = p_0 = \text{const}$, as shown in Figure 1. This case applies to stationary values of the rates $a(t) = a_0$, $b(t) = b_0$, $\beta = \beta_0$ and $c(t) = c_0$ as well as to any time-dependent star formation rate $a(t)$, provided $b(t) \propto a(t)$, $\beta(t) \propto a(t)$, and $c(t) \propto a(t)$ have the same time variation while their absolute values can be different.

It is appropriate to introduce the dimensionless reduced time variable.

$$\tau = \int_{t_0}^{t} d\xi\, a(\xi) = a_0(t - t_0) \tag{8}$$

in terms of the stationary triggered star formation rate a_0. This reduced time scale differs from the one introduced in part I: $\tilde{t} = \beta_0(t - t_0)$. Obviously, for stationary rates the relation

$$\tau = \frac{a_0}{\beta_0}\tilde{t} \tag{9}$$

holds. In a flat ΛCDM Friedmann cosmology with $\Omega_m = 0.3$ and the Hubble constant $H_0 = 70h_{70}$ km s^{-1} Mpc^{-1} the relation (9) implies with Equations (I-42) (Throughout this manuscript the notation (I-x) refers to Equation (x) in part I of the present study, see [1]) the redshift dependency (for details see Appendix A)

$$\tau(z) \simeq \frac{\phi(z)}{(1+z)^{3/2}}, \quad \phi(z) = \phi\zeta(z), \quad \phi = \frac{5.37\,\tilde{a}_0}{h_{70}}, \tag{10}$$

$$\zeta(z) = \frac{(1+z)^{3/2}}{\sqrt{\frac{7}{3} + (1+z)^3}} \simeq 1 - \left(1 - \sqrt{\frac{3}{10}}\right) e^{-4z/3}, \tag{11}$$

$$\zeta(0) = \sqrt{0.3} = 0.548. \tag{12}$$

In the following, the modification introduced by the factor (11) entered only in Section 7 to calculate the present-day quantities at redshift $z = 0$ whereas for finite redshift we set $\zeta(z) = 1$. In Equation (10) the triggered star formation rate is scaled as

$$a_0 = 10^{-17}\tilde{a}_0 \text{ Hz}. \tag{13}$$

with dimensionless $\tilde{a}_0$ (using traditional non-SI units, 10^{-17} Hz ≈ 0.315/Gyr). The Equations (1)–(3) including the redundant Equation (4) then read

$$1 = G(\tau) + S(\tau) + L(\tau), \tag{14a}$$

$$\frac{dG}{d\tau} = -G(\tau)S(\tau) - q_0 G(\tau) + k_0 S(\tau), \tag{14b}$$

$$\frac{dS}{d\tau} = G(\tau)S(\tau) + q_0 G(\tau) - [k_0 + p_0]S(\tau), \tag{14c}$$

$$\frac{dL}{d\tau} = p_0 S(\tau), \tag{14d}$$

obeying the initial conditions

$$G(\tau = 0) = 1, \qquad S(\tau = 0) = 0, \qquad L(\tau = 0) = 0. \tag{15}$$

In Equation (14), we introduced the dimensionless constant ratios

$$k_0 = \frac{b_0}{a_0}, \qquad q_0 = \frac{\beta_0}{a_0}, \qquad p_0 = \frac{c_0}{a_0}, \tag{16}$$

and the formation rate of new stars (6) as a function of reduced time is given by

$$j(\tau) = G(\tau)S(\tau) + q_0 G(\tau). \tag{17}$$

At $\tau = \infty$ Equation 14 attains a stationary state where all time derivatives vanish. For finite $p_0 > 0$ Equation (14d) then implies $S_\infty = 0$, so that $G_\infty = 0$ according to Equation (14b) leading to $L(\infty) = 1$ according to the sum constraint (14a). For later use, we thus note

$$G_\infty = S_\infty = 0, \qquad L(\infty) = 1. \tag{18}$$

Equations (14) could be simplified upon introducing

$$M(\tau) = G(\tau) - k_0, \qquad N(\tau) = S(\tau) + q_0. \tag{19}$$

Using $M(\tau)$ and $N(\tau)$ yielded for Equations (14)

$$\begin{aligned}
\frac{dM}{d\tau} &= -M(\tau)N(\tau) - q_0 k_0, && \text{(20a)}\\
\frac{dN}{d\tau} &= M(\tau)N(\tau) + q_0 k_0 - p_0[N(\tau) - q_0], && \text{(20b)}\\
\frac{dL}{d\tau} &= p_0[N(\tau) - q_0], && \text{(20c)}\\
1 &= M(\tau) + N(\tau) + L(\tau) + k_0 - q_0, && \text{(20d)}
\end{aligned}$$

with the initial conditions

$$M(\tau = 0) = 1 - k_0, \qquad N(\tau = 0) = q_0, \qquad L(\tau = 0) = 0. \tag{21}$$

In the following two sections, we investigated analytical solutions of Equations (20) and (21): first, for the special GS-case of negligible stellar evolution ($c_0 = p_0 = 0$) in Section 3, before we investigated the general GSL-case (Section 4).

3. GS-Limit For Negligible Stellar Evolution

In the case of vanishing stellar evolution, $c_0 = p_0 = 0$, implying $L(\tau) = 0$ at all times (Figure 1). In that case the reduced GSL model Equations (14b) and (14c) and (14a) simplified to the GS model equation

$$\begin{aligned}
\frac{dG}{d\tau} &= -G(\tau)S(\tau) - q_0 G(\tau) + k_0 S(\tau), && \text{(22a)}\\
\frac{dS}{d\tau} &= G(\tau)S(\tau) + q_0 G(\tau) - k_0 S(\tau), && \text{(22b)}\\
G(\tau) + S(\tau) &= 1, && \text{(22c)}
\end{aligned}$$

so that with Equations (19) we obtained

$$\begin{aligned}
\frac{dM}{d\tau} &= -M(\tau)N(\tau) - q_0 k_0, && \text{(23a)}\\
\frac{dN}{d\tau} &= M(\tau)N(\tau) + q_0 k_0. && \text{(23b)}
\end{aligned}$$

Equation (23a) readily provided

$$N(\tau) = -\frac{\frac{dM}{d\tau} + k_0 q_0}{M(\tau)}, \tag{24}$$

so that

$$S(\tau) = -q_0 - \frac{\frac{d(G(\tau)-k_0)}{d\tau} + k_0 q_0}{G(\tau) - k_0} = -q_0 - \frac{\frac{dG(\tau)}{d\tau} + k_0 q_0}{G(\tau) - k_0}. \tag{25}$$

Upon insertion of Equation (25) the sum constraint (22c) became

$$1+q_0 = G(\tau) - \frac{\frac{dG(\tau)}{d\tau}+k_0 q_0}{G(\tau)-k_0}, \tag{26}$$

or equivalently,

$$\frac{dG(\tau)}{d\tau} = G^2(\tau) - (1+q_0+k_0)G(\tau) + k_0. \tag{27}$$

According to Equation (27) the fraction $G(\tau)$ approaches a stationary value G_∞ at $\tau \to \infty$, which is given by

$$\begin{aligned} G_\infty &= \frac{1}{2}(\chi_0 - \omega_0) \\ &= \frac{1}{2}[1+q_0+k_0 - \sqrt{(1+q_0)^2 + k_0^2 - 2k_0(1-q_0)}], \end{aligned} \tag{28}$$

where

$$\chi_0 \equiv 1+k_0+q_0 > 1, \qquad \omega_0 \equiv \sqrt{\chi_0^2 - 4k_0} \geq 0. \tag{29}$$

Taking into account the initial conditions (15), the solution of Equation (27) could be written as

$$\begin{aligned} \tau &= \int_1^{G(\tau)} \frac{dx}{x^2 - (1+q_0+k_0)x + k_0} \\ &= -\int_1^{G(\tau)} \frac{dx}{(x-G_\infty)(\chi_0 - G_\infty - x)} \\ &= -\int_{1-G_\infty}^{G(\tau)-G_\infty} \frac{dy}{y(\chi_0 - 2G_\infty - y)} \\ &= -\frac{1}{\omega_0}\int_{1-G_\infty}^{G(\tau)-G_\infty} dy \left[\frac{1}{y} + \frac{1}{\omega_0 - y}\right]. \end{aligned} \tag{30}$$

This integral is evaluated to

$$\omega_0\tau = -\left[\ln\frac{y}{\omega_0-y}\right]_{1-G_\infty}^{G-G_\infty} = \left[\ln\left(\frac{\omega_0}{y}-1\right)\right]_{1-G_\infty}^{G-G_\infty} = \ln\frac{\frac{\omega_0}{G-G_\infty}-1}{\frac{\omega_0}{1-G_\infty}-1}, \tag{31}$$

or equivalently

$$G(\tau) = G_\infty + \frac{\omega_0}{1+\left(\frac{\omega_0}{1-G_\infty}-1\right)e^{\omega_0\tau}}. \tag{32}$$

The sum constraint (22c) then readily yielded

$$S(\tau) = 1 - G(\tau) = 1 - G_\infty - \frac{\omega_0}{1+\left(\frac{\omega_0}{1-G_\infty}-1\right)e^{\omega_0\tau}}, \tag{33}$$

providing

$$S_\infty = 1 - G_\infty = \frac{1}{2}\left[1 - q_0 - k_0 + \sqrt{(1+q_0)^2 + k_0^2 - 2k_0(1-q_0)}\right]. \tag{34}$$

Consequently, the dimensionless star formation rate (17) became

$$j(\tau) = G(\tau)[S(\tau)+q_0] = \left[G_\infty + \frac{\omega_0}{1+\left(\frac{\omega_0}{1-G_\infty}-1\right)e^{\omega_0\tau}}\right]\left[1+q_0-G_\infty - \frac{\omega_0}{1+\left(\frac{\omega_0}{1-G_\infty}-1\right)e^{\omega_0\tau}}\right] \tag{35}$$

where we recall that ω_0 and G_∞ are both known in terms of k_0 and q_0. The maximum of $j(\tau)$ is attained at τ_j solving $dj(\tau)/d\tau = 0$. This yielded the dimensionless peak time

$$\tau_j = \frac{1}{\omega_0}\ln\left[\frac{1+q_0-2(G_\infty+\omega_0)}{\left(\frac{\omega_0}{1-G_\infty}-1\right)(2G_\infty - q_0 - 1)}\right], \tag{36}$$

as well, upon inserting τ_j into Equation (35), the peak amplitude

$$j_{\max} = \frac{(1+q_0)^2}{4}, \tag{37}$$

where we made use of the definitions of χ_0, ω_0, and G_∞ according to Equation (28) to simplify the final expression. For the present case of $p_0 = 0$ the analytical solutions (32), (33), (35) are shown to be identical with the numerical solution in Figure 2 for various choices of q_0 and k_0. Following [33] the numerical solution of the GSL equations we obtained using the 10th order predictor–corrector Adams method [34,35]. Within 0.1% precision, a single-step solver based on a modified Rosenbrock formula of order 2, implemented by [36] as ode23s in Matlab$^{\mathrm{TM}}$ yielded practically indistinguishable results. The excellent agreement between the numerical and analytical solutions in Figure 2 confirms the validity of our derivations.

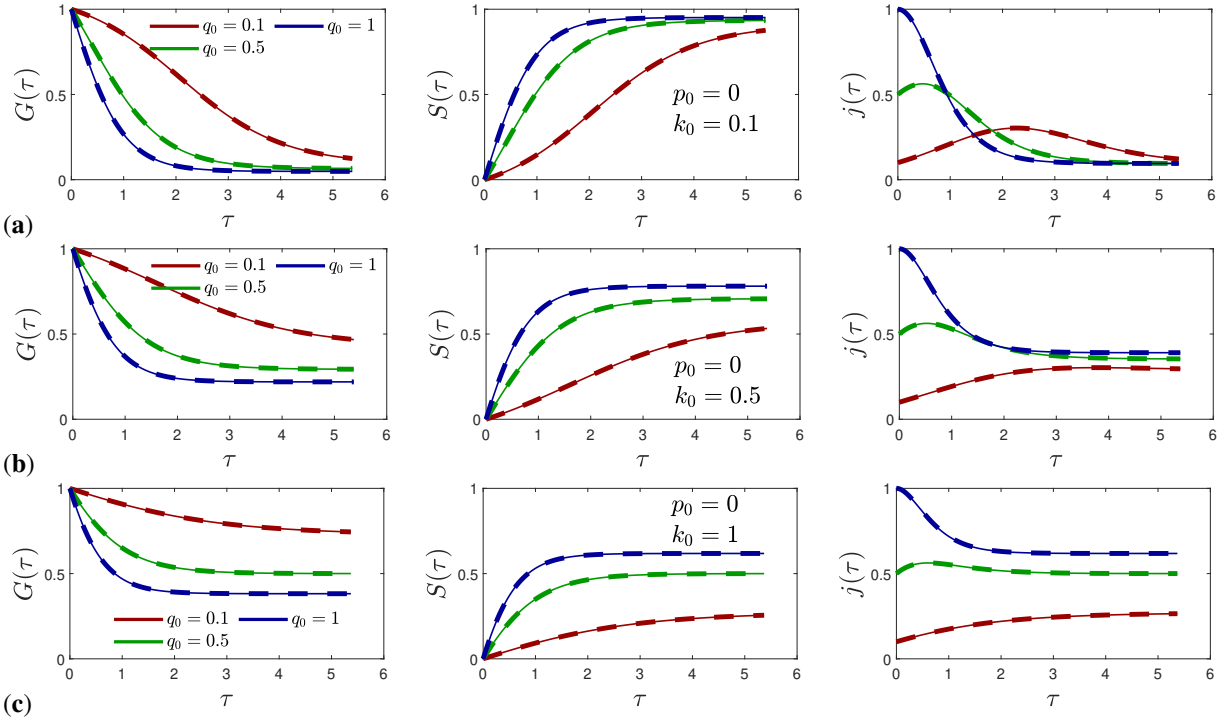

Figure 2. GS model. Numerical solution (thin solid line) and analytical solution, Equations (32), (33), and (35) (thick dashed line) for the GS-limit with negligible stellar evolution ($p_0 = 0$). Shown are (left) $G(\tau)$, (middle) $S(\tau)$ and (right) $j(\tau)$ versus dimensionless τ for the cases of (**a**) $k_0 = 0.1$, (**b**) $k_0 = 0.5$, and (**c**) $k_0 = 1$. Each panel displays curves for $q_0 \in \{0.1, 0.5, 1.0\}$.

4. The Full GSL Model for Stationary Ratios

For the full GSL-model including stellar evolution $p_0 > 0$ the Equations (20) are further reduced in Appendix B. Introducing

$$U(\tau) = \int_0^\tau d\tau' M(\tau') - p_0\tau, \tag{38}$$

$$M(\tau) = G(\tau) - k_0 = \frac{dU(\tau)}{d\tau} + p_0 \tag{39}$$

It is demonstrated there that the full GSL-equations are equivalent to an exact determining nonlinear integro-differential equations for the function $U(\tau)$ reading (see Equation (A35))

$$\frac{dU(\tau)}{d\tau} + q_0 e^{U(\tau)} \left(1 + (k_0 + p_0)\int_0^\tau dx\, e^{-U(x)}\right) = \epsilon + p_0 e^{-p_0\tau} \int_0^\tau dx\, e^{p_0 x} \left[\frac{dU(x)}{dx} - \left(\frac{dU}{dx}\right)_{x=0}\right]. \tag{40}$$

with ϵ defined by

$$\epsilon = 1 + q_0 - (p_0 + k_0). \tag{41}$$

In the Section 5 we solve Equation (A35) approximately.

5. Approximate Solutions of Equation (40)

5.1. Ansatz

The ansatz

$$Y(\tau) = e^{-U(\tau)} = c_1 e^{\alpha_1 \tau} + (1 - c_1) e^{\alpha_2 \tau}, \tag{42}$$

where without loss of generality $\alpha_1 > \alpha_2$, ensures that $U(0) = 0$ and implies

$$U'(\tau) = -\alpha_1 - \frac{(1-c_1)(\alpha_2 - \alpha_1) e^{(\alpha_2 - \alpha_1)\tau}}{c_1 + (1-c_1) e^{(\alpha_2 - \alpha_1)\tau}} = -\alpha_1 + \frac{\alpha_1 - \alpha_2}{\frac{c_1}{1-c_1} e^{(\alpha_1 - \alpha_2)\tau} + 1}. \tag{43}$$

The constants c_1, α_1 and α_2 will be determined later. We wrote Equation (A35) as

$$\frac{dU(\tau)}{d\tau} + q_0 e^{U(\tau)} \left(1 + (k_0 + p_0) \int_0^\tau dx\, e^{-U(x)} \right) = \epsilon + R(\tau), \tag{44}$$

with

$$R(\tau) = p_0 e^{-p_0 \tau} \int_0^\tau dx\, e^{p_0 x} [U'(x) - U'(0)]. \tag{45}$$

By multiplying with $e^{-U(\tau)}$, the Equation (44) in terms of $Y(\tau) = e^{-U(\tau)}$ reads

$$\frac{dY(\tau)}{d\tau} + [\epsilon + R(\tau)] Y(\tau) - q_0 (k_0 + p_0) \int_0^\tau dx\, Y(x) = q_0, \tag{46}$$

which is still exact.

5.1.1. Small Times

For small times $\tau \ll p_0^{-1}$, where $U'(\tau) \simeq U'(0)$, the function (45) vanishes

$$R(\tau \leq p_0^{-1}) \simeq R(\tau = 0) = 0, \tag{47}$$

which in the special case of vanishing stellar evolution ($p_0 = 0$) holds at all times. The next subsection investigates the solution at small times using the approximation (47).

5.1.2. Parameter Relation For Non-Zero Values $p_0 \neq 1$

For finite values of p_0 we noted that with the limits (A37) and (A43) Equation (44) for $\tau = \infty$ provides

$$\epsilon + R(\infty) = U'(\infty) - \frac{q_0 (p_0 + k_0)}{U'(\infty)} = -(p_0 + k_0) + q_0, \tag{48}$$

so that

$$R(\infty) = q_0 - (p_0 + k_0) - \epsilon = -1. \tag{49}$$

According to Equation (43)

$$U'(x) - U'(0) = (\alpha_1 - \alpha_2) \left[\frac{1}{\frac{c_1}{1-c_1} e^{(\alpha_1 - \alpha_2)x} + 1} - (1 - c_1) \right], \tag{50}$$

so that Equation (45) became

$$R(\tau) = p_0 (\alpha_1 - \alpha_2) e^{-p_0 \tau} \left(\int_0^\tau dx\, \frac{e^{p_0 x}}{\frac{c_1}{1-c_1} e^{(\alpha_1 - \alpha_2)x} + 1} - (1 - c_1) \int_0^\tau dx\, e^{p_0 x} \right). \tag{51}$$

Substituting $y = e^{(\alpha_1-\alpha_2)\tau}$ allowed us to express the function (51) in terms of the hypergeometric ${}_2F_1$ function

$$\begin{aligned} R(\tau) &= p_0(\alpha_1-\alpha_2)e^{-p_0\tau}\left[\frac{1}{\alpha_1-\alpha_2}\int_1^{e^{(\alpha_1-\alpha_2)\tau}} dy\,\frac{y^{\mu-1}}{1+\frac{c_1}{1-c_1}y} - \frac{1-c_1}{p_0}(e^{p_0\tau}-1)\right] \\ &= (\alpha_1-\alpha_2)\Big\{{}_2F_1\left(1,\mu;1+\mu;-\frac{c_1}{1-c_1}e^{(\alpha_1-\alpha_2)\tau}\right) - (1-c_1) \\ &\quad -e^{-p_0\tau}\left[{}_2F_1\left(1,\mu;1+\mu;-\frac{c_1}{1-c_1}\right) - (1-c_1)\right]\Big\}, \end{aligned} \tag{52}$$

with $\mu = p_0/(\alpha_1-\alpha_2)$. With the help of the linear transformation formula ([37])

$${}_2F_1(a,b;c;z) = (1-z)^{-a}\,{}_2F_1\left(a,c-b;c;\frac{z}{z-1}\right), \tag{53}$$

we found for Equation (52)

$$\begin{aligned} R(\tau) &= (\alpha_1-\alpha_2)(1-c_1)\Big[\frac{{}_2F_1\left(1,1;1+\mu;\frac{1}{1+\frac{1-c_1}{c_1}e^{(\alpha_2-\alpha_1)\tau}}\right)}{1+\frac{c_1}{1-c_1}e^{(\alpha_1-\alpha_2)\tau}} - 1 \\ &\quad - e^{-p_0\tau}\Big({}_2F_1(1,1;1+\mu;c_1) - 1\Big)\Big], \end{aligned} \tag{54}$$

indicating that for infinitely large times

$$R(\infty) = -(\alpha_1-\alpha_2)(1-c_1). \tag{55}$$

The function $R(\tau)$ is negative and monotonically decreases with τ. Equating the two limits (49) and (55) then required

$$1-c_1 = (\alpha_1-\alpha_2)^{-1}, \qquad c_1 = 1-\frac{1}{\alpha_1-\alpha_2}. \tag{56}$$

With this choice, we obtained for Equation (43)

$$U'(\tau) = -\alpha_1 + \frac{1}{1-c_1+c_1e^{\frac{\tau}{1-c_1}}}, \tag{57}$$

implying immediately for $0 < c_1 < 1$

$$U'(0) = 1-\alpha_1, \quad U'(\infty) = -\alpha_1, \tag{58}$$

so that with

$$\alpha_1 = p_0 + k_0 \tag{59}$$

the initial (A24) and final conditions (A43) for $U'(0)$ are exactly fulfilled. Consequently, Equation (57) reads

$$U'(\tau) = -(p_0+k_0) + \frac{1}{1-c_1+c_1e^{\frac{\tau}{1-c_1}}}, \tag{60}$$

depending on the single parameter c_1. Equation (60) is used in subsection to derive an approximate solution for all times. However, we emphasize that the relation (56) between c_1 and $\alpha_1-\alpha_2$, respectively, and therefore Equation (60) are valid only for finite values of p_0 and $R(\tau)$.

5.2. Approximate Solution For Small Times

With the approximation (47) the ansatz (42) exactly solves Equation (46) being equivalent to

$$\frac{dY(\tau)}{d\tau} + \epsilon Y(\tau) - q_0(k_0+p_0)\int_0^\tau dx\,Y(x) = q_0, \tag{61}$$

if

$$\alpha_1 = \frac{\omega-\epsilon}{2}, \quad \alpha_2 = -\frac{\omega+\epsilon}{2} = \alpha_1-\omega, \tag{62}$$

with

$$\omega = \sqrt{\epsilon^2 + 4q_0(k_0 + p_0)} \geq \epsilon \tag{63}$$

and

$$c_1\alpha_2 + (1 - c_1)\alpha_1 = \alpha_1 - \omega c_1 = \frac{\alpha_1\alpha_2}{p_0 + k_0} = \frac{\epsilon^2 - \omega^2}{4(p_0 + k_0)} = -q_0, \tag{64}$$

providing

$$c_1 = \frac{\omega - \epsilon + 2q_0}{2\omega}, \quad \alpha = \frac{c_1}{1 - c_1} = \frac{\omega - \epsilon + 2q_0}{\omega + \epsilon - 2q_0}. \tag{65}$$

The solution (42) then became

$$Y(\tau) = c_1 e^{\alpha_1 \tau}[1 + \alpha^{-1} e^{-\omega\tau}], \tag{66}$$

implying

$$U_s(\tau) = -\ln Y(\tau) = -\ln(c_1) + \frac{\epsilon - \omega}{2}\tau - \ln\left[1 + \alpha^{-1} e^{-\omega\tau}\right], \tag{67}$$

and

$$U_s'(\tau) = \frac{\epsilon - \omega}{2} + \frac{\omega}{1 + \alpha e^{\omega\tau}}, \tag{68}$$

so that

$$\begin{aligned} G_s(\tau) &= k_0 + p_0 + \frac{\epsilon - \omega}{2} + \frac{\omega}{1 + \alpha e^{\omega\tau}} \\ &= \frac{1 + p_0 + k_0 + q_0}{2} - \frac{\omega}{2}\tanh\frac{\omega\tau + \ln\alpha}{2}. \end{aligned} \tag{69}$$

with ω and ϵ given by Equations (63) and (41), respectively. Here, the subscript s indicates that we consider the small time limit. Equations (67)–(69) correctly reproduce $U_s(0) = 0$, $U_s'(0) = \epsilon - q_0 = 1 - (k_0 + p_0)$ and $G_s(0) = 1$.

In Figure 3 we compared the resulting fractions $G_s(\tau)$ with the numerically calculated ones for several different choices of the parameters p_0, k_0 and q_0. The agreement is reasonably good for small times, but fails at large times. We therefore considered a modified approximate approach valid at all times in SubSection 5.3. In Appendix C we note an important feature of the present solution for vanishing $p_0 = 0$.

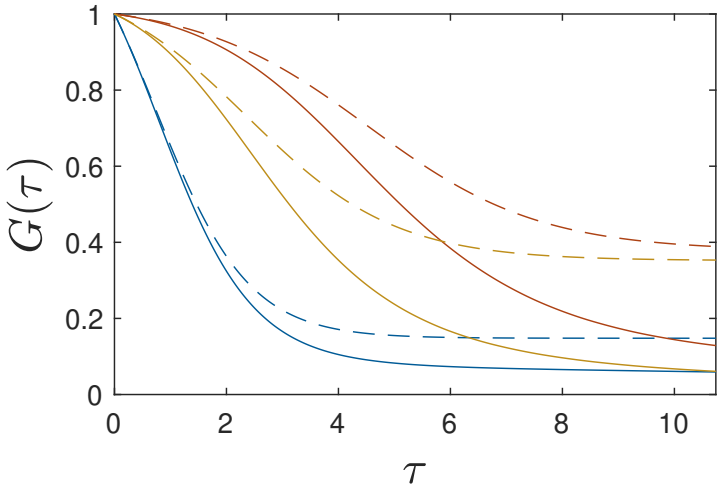

Figure 3. GSL model. Fraction $G_s(\tau)$ (dashed) compared with the numerically calculated $G(\tau)$ (solid) for several choices of the parameters p_0, k_0, and q_0: (blue) $k_0 = 0.1$, $p_0 = 0.1$, $q_0 = 0.3$, (red) $k_0 = 0.02$, $p_0 = 0.37$, $q_0 = 0.02$, and (yellow) $k_0 = 0.02$, $p_0 = 0.37$, $q_0 = 0.07$. The numerical $G(\tau)$ approaches zero in the limit $\tau \to \infty$, while the small time approximation $G_s(\tau)$ (69) remains finite. Note that the shown analytical curves $G_s(\tau)$ in the small time approximation agree with those in Figure 2.

5.3. Modified Approximation For General Times

For non-zero values of $p_0 > 0$ we used the earlier derived Equation (60) based on relation (56) to obtain for the gas fraction

$$G(\tau) = k_0 + p_0 + U'(\tau) = \frac{1}{1 - c_1 + c_1 e^{\frac{\tau}{1 - c_1}}}. \tag{70}$$

We noted before that with the relation (56) the initial and final conditions for $U'(\tau)$ are fulfilled, as can also be seen from Equation (70) yielding $G(0) = G_\infty = 0$. Equation (70) readily provided

$$G'(\tau) = U''(\tau) = -\frac{c_1 e^{\frac{\tau}{1-c_1}}}{(1-c_1)[1-c_1+c_1 e^{\frac{\tau}{1-c_1}}]^2}. \tag{71}$$

To determine the remaining parameter c_1 we here used the exact condition (A24) for $G'(0) = -q_0$ yielding

$$\frac{c_1}{1-c_1} = q_0, \tag{72}$$

so that

$$\begin{aligned} c_1 &= \frac{q_0}{1+q_0}, \qquad \alpha_2 = p_0 + k_0 - 1 - q_0 = -\epsilon, \\ \alpha_1 &= p_0 + k_0, \qquad \epsilon = 1 + q_0 - (p_0 + k_0) \end{aligned} \tag{73}$$

We then found for the gas fraction (70)

$$G(\tau) = \frac{1+q_0}{1+q_0 e^{(1+q_0)\tau}} = \frac{1+q_0}{1+e^{(1+q_0)(\tau-\tau_G)}}, \tag{74}$$

shown in Figure 4, with

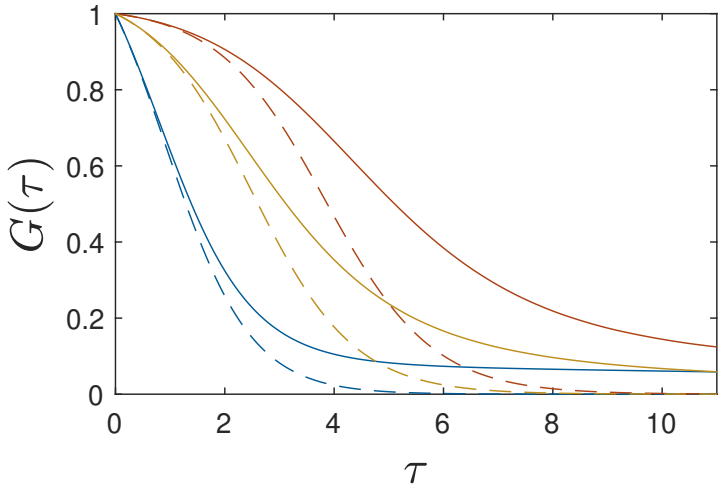

Figure 4. GSL model. Fraction $G(\tau)$ according to Equation (74) (dashed) compared with the numerically calculated $G(\tau)$ (solid) for the same choices of parameters as in Figure 2. Both the numerical $G(\tau)$ and the approximation approach zero in the limit $\tau \to \infty$.

$$\tau_G = -\frac{\ln q_0}{1+q_0}. \tag{75}$$

This timescale is solely determined by the ratio q_0 of spontaneous to triggered star formation. Likewise, Equation (42) reads

$$Y(\tau) = \frac{q_0 e^{\alpha_1 \tau} + e^{-\epsilon\tau}}{1+q_0}, \tag{76}$$

providing for the luminous stellar matter fraction (A21)

$$\begin{aligned} \frac{S(\tau)+q_0}{q_0} &= \frac{1+(k_0+p_0)\int_0^\tau dx\, Y(x)}{Y(\tau)} = \frac{1+q_0 e^{\alpha_1\tau} + \frac{\alpha_1}{\epsilon}(1-e^{-\epsilon\tau})}{q_0 e^{\alpha_1\tau} + e^{-\epsilon\tau}} \\ &= 1 + \frac{(1+\frac{\alpha_1}{\epsilon})(1-e^{-\epsilon\tau})}{q_0 e^{\alpha_1\tau} + e^{-\epsilon\tau}}, \end{aligned} \tag{77}$$

so that

$$\begin{aligned} S(\tau) &= \frac{q_0(\alpha_1+\epsilon)[1-e^{-\epsilon\tau}]}{\epsilon[q_0 e^{\alpha_1\tau}+e^{-\epsilon\tau}]} = \frac{q_0(1+q_0)[1-e^{-\epsilon\tau}]}{\epsilon[q_0 e^{\alpha_1\tau}+e^{-\epsilon\tau}]} \\ &= \frac{q_0(1+q_0)[e^{\epsilon\tau}-1]}{\epsilon[q_0 e^{(1+q_0)\tau}+1]} = \frac{q_0(1+q_0)[e^{\epsilon\tau}-1]}{\epsilon[1+e^{(1+q_0)(\tau-\tau_G)}]} = \frac{q_0[e^{\epsilon\tau}-1]}{\epsilon} G(\tau), \end{aligned} \tag{78}$$

which correctly reproduces $S(0) = S_\infty = 0$. The first derivative of the fraction (78) vanishes at the time τ_S given by the solution of the Eq.

$$[q_0 e^{(1+q_0)\tau_S}+1]\epsilon e^{\epsilon\tau_S} = q_0(1+q_0)e^{(1+q_0)\tau_S}[e^{\epsilon\tau_S}-1], \tag{79}$$

leading to

$$(p_0+k_0)e^{(1+q_0)\tau_S} - (1+q_0)e^{(p_0+k_0)\tau_S} = \frac{\epsilon}{q_0}. \tag{80}$$

As the first term dominates the left-hand side of the last Equation we obtained approximately.

$$\tau_S \simeq \frac{1}{1+q_0}\left(-\ln(q_0) + \ln\frac{\epsilon}{p_0+k_0}\right) = \tau_G + \frac{\ln\frac{\epsilon}{p_0+k_0}}{1+q_0}, \tag{81}$$

which is slightly larger than the time scale (75). Replacing τ in Equation (78) by τ_S from Equation (81) we found for the peak stellar matter ratio

$$S_{\max} = S(\tau_S) \simeq e^{-(p_0+k_0)\tau_S} \simeq \left[\frac{q_0(1+q_0)}{1+q_0-p_0-k_0}\right]^{\frac{p_0+k_0}{1+q_0}}. \tag{82}$$

According to Equations (14b) and (17) one has

$$j(\tau) = -\frac{dG(\tau)}{d\tau} + k_0 S(\tau), \tag{83}$$

where

$$-\frac{dG(\tau)}{d\tau} = -U''(\tau) = \frac{(1+q_0)^2}{4\cosh^2\frac{(1+q_0)(\tau-\tau_G)}{2}}. \tag{84}$$

For small values of k_0, that is $k_0 \ll 1$,

$$k_0 S(\tau) \le k_0 S_{\max} \simeq k_0\left[\frac{q_0(1+q_0)}{1+q_0-p_0-k_0}\right]^{\frac{p_0+k_0}{1+q_0}} \tag{85}$$

is negligibly smaller than $|G'(\tau)|$, so that the formation rate of new stars (83) reduced to

$$j(\tau) \simeq -G'(\tau) = \frac{(1+q_0)^2}{4\cosh^2\frac{(1+q_0)(\tau-\tau_G)}{2}}. \tag{86}$$

This formation rate attains its maximum value.

$$j_{\max} = \left(\frac{1+q_0}{2}\right)^2 \tag{87}$$

at the peak time $\tau_j \simeq \tau_G$, where τ_G is was introduced in Equation (75). Most noteworthy, both the maximum value and the peak time are solely determined by the ratio q_0 of the spontaneous to triggered star formation rates, whereas the two other ratios p_0 and k_0 do not enter here.

Finally, the fraction of locked-in matter followed from the sum constraint as

$$\begin{aligned} L(\tau) &= 1 - G(\tau) - S(\tau) \\ &= 1 - \frac{1+q_0}{1+e^{(1+q_0)(\tau-\tau_G)}} - \frac{q_0(1+q_0)[e^{\epsilon\tau}-1]}{\epsilon[q_0 e^{(1+q_0)\tau}+1]} \\ &= 1 - \frac{1+q_0}{1+e^{(1+q_0)(\tau-\tau_G)}}\left[1+\frac{q_0(e^{\epsilon\tau}-1)}{\epsilon}\right], \end{aligned} \tag{88}$$

where we inserted Equations (74) and (78). The derived expressions (74), (78), and (88) for $G(\tau)$, $S(\tau)$, and $L(\tau)$ were used in the following sections.

6. Cosmic Star Formation History

As in part I, we consider the cosmic star formation history (SFH) of the universe, which is proportional to the star formation rate (6). In the following, the SFR density and the integrated stellar density using our results from the earlier Section 5.3 are calculated, and compared with data at redshifts up to $z = 6$ collected by [38]—see also ref. [39]. Recent James Webb Space Telescope (JWST) observations [40] will contribute more data at large redshifts $z > 6$.

According to Equations (I-46) and (I-47) as well as Equations (9) and (10) for general $j(\tau)$, the theoretical cosmic SFR density and the integrated stellar density as a function of redshift are

$$\psi_{\rm GSL}(z) = A_1 \frac{j(\tau(z))}{(1+z)^{5/2}} \tag{89}$$

with

$$A_1 = 2.78 \cdot 10^{-10} a_0^2 h_{70} = 2.78 \cdot 10^{-44} \tilde{a}_0^2 h_{70}\ \mathrm{kg\,m^{-3}\,s}, \tag{90}$$

and

$$\begin{aligned} \rho^*_{\rm GSL}(z) &= B_1 \int_z^{1100} dz'\,[1 - L(z') - G(z')] \frac{j(\tau(z'))}{(1+z')^5} \\ &= B_1 \int_z^{1100} dz'\, S(z') \frac{j(\tau(z'))}{(1+z')^5}, \end{aligned} \tag{91}$$

with

$$B_1 = 2.24 \cdot 10^8 a_0^2 = 2.24 \cdot 10^{-26} \tilde{a}_0^2\ \mathrm{kg\ m^{-3}}. \tag{92}$$

In part I we have argued that the factor $1 - L(z)$ enters the calculation of $\rho^*_{\rm GSL}(z)$ but not the calculation of the SFR density (89) because all stars are born as luminous main sequence stars but only the fraction $1-L(z)$ contributes to the observed integrated density of luminous stars. Here we refined this reduction factor to $1-L(z)-G(z) = S(z)$ as the baryonic gas does not contribute to the integrated luminous stellar density.

6.1. Observational Constraints

For the comparison with the predictions of the GSL-model, we required the same five constraints as in part I. First, the observed peak SFR density is given by

$$\psi(z_E) = 0.178^{+0.372}_{-0.044}\ M_\odot \mathrm{yr}^{-1}\mathrm{Mpc}^{-3} = (3.83^{+8.00}_{-0.95}) \cdot 10^{-46}\ \mathrm{kg\ s^{-1}\ m^{-3}}, \tag{93}$$

and occurs in the redshift range 1.62–1.88 ([41]) and 1.7–2.5 ([42]). Secondly, we required the observed peak redshift.

$$z_E = 2.0 \pm 1.0. \tag{94}$$

As the third constraint we used the observed integrated stellar mass density at $z = 0$ ([43,44])

$$\rho^*(0) = (5.62^{+1.79}_{-1.35}) \cdot 10^8\ \frac{M_\odot}{\mathrm{Mpc}^3} = (3.80^{+1.21}_{-0.91}) \cdot 10^{-29}\ \mathrm{kg\ m^{-3}} \tag{95}$$

As the fourth constraint we demanded that $(d\psi/dz)_{z=0} > 0$ in order to have at least one maximum of $\psi(z)$ at positive z. As the fifth more stringent constraint we required that $\psi_{\rm GSL}(z)$ exhibits exactly one maximum within the redshift range $z \in [0, 8]$.

6.2. SFR Density

Using Equation (86) for $j(\tau)$ and Equation (10) for $\tau(z)$ the SFR density (89) became

$$\psi_{\rm GSL}(\tau(z)) = \frac{A_1 (1+q_0)^2 \Psi(\tau)}{4\phi^{5/3}}, \tag{96a}$$

$$\Psi(\tau) = \frac{\tau^{5/3}}{\cosh^2 \frac{(1+q_0)(\tau-\tau_G)}{2}}. \tag{96b}$$

This SFR density (96) fulfills the fourth and fifth constraint mentioned in the last Subsection 6.1. With the first derivative

$$\frac{d\Psi(\tau)}{d\tau} = \frac{5}{3}\frac{\tau^{2/3}}{\cosh^2\frac{(1+q_0)(\tau-\tau_G)}{2}}\left[1-\frac{3}{5}(1+q_0)\tau\tanh\frac{(1+q_0)(\tau-\tau_G)}{2}\right] \tag{97}$$

we found that a single maximum occurs at τ_E given by the solution of the transcendental equation

$$\tanh\frac{(1+q_0)(\tau_E-\tau_G)}{2} = \frac{5}{3(1+q_0)\tau_E}, \tag{98}$$

while

$$\Psi_{\max} = \tau_E^{-1/3}\left[\tau_E^2 - \frac{25}{9(1+q_0)^2}\right]. \tag{99}$$

Using the following abbreviations,

$$X = \frac{(1+q_0)\tau_E}{2}, \quad X_u = \frac{(1+q_0)\tau_G}{2} = -\frac{\ln q_0}{2}, \tag{100}$$

Equation (98) simplified to

$$\tanh(X - X_u) = \frac{5}{6X}. \tag{101}$$

To solve Equation (101) one has to discriminate between the cases of positive and negative X_u, which correspond to values of q_0 small and large compared to unity.

For values of $0 \le X_u < 3$, corresponding to $e^{-6} = 2.48\cdot 10^{-3} \le q_0 \le 1$, the positive solution of Equation (101) with a maximum relative deviation of 0.9% from the exact solution is given by

$$\begin{aligned} X(q_0 \le 1) &= \frac{(1+q_0)\tau_E}{2} \simeq 1.06\left(1+\frac{X_u^{1.3}}{2}\right) \\ &\simeq 1.06\left[1+0.192\,(-\ln q_0)^{1.3}\right], \end{aligned} \tag{102}$$

where $X \simeq 1.06$ is the numerical solution of $\tanh(X) = 5/(6X)$. Values $q_0 \in [0.01, 1]$ correspond to values of $X_u \in [0, 2.3]$. For values $X_u < 0$, corresponding to values of $q_0 > 1$, the positive solution of Equation (101) with a maximum relative deviation of 0.4% from the exact solution is given by

$$\begin{aligned} X(q_0 > 1) &\simeq \frac{5}{6} + \left(1.06 - \frac{5}{6}\right)e^{5X_u/3} \\ &= \frac{5}{6}[1 + 0.272e^{5X_u/3}] = \frac{5}{6}\left[1+\frac{0.272}{q_0^{5/6}}\right]. \end{aligned} \tag{103}$$

This approximation is exact at $X_u = 0$ and $X_u \to -\infty$, and compared with the numerical solution in Figure 5. The cases $q_0 \le 1$ and $q_0 > 1$ will be discussed in turn.

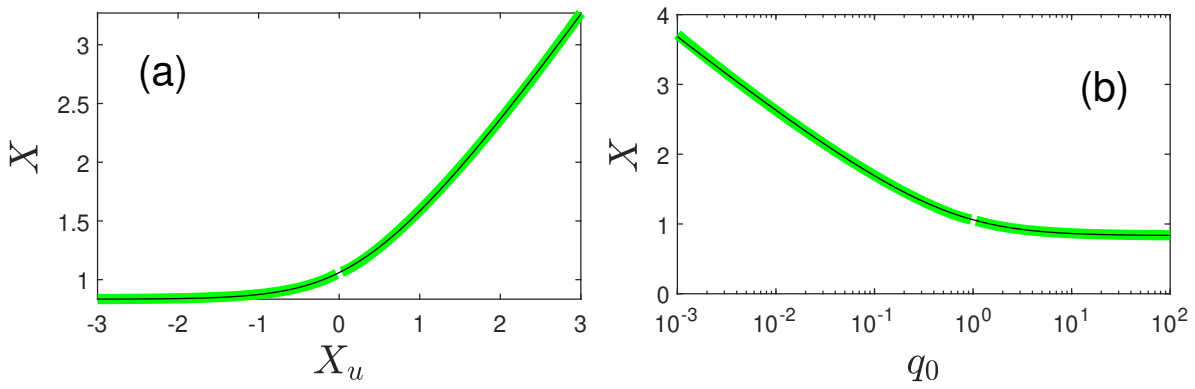

Figure 5. Approximate solution of transcendental equation. Exact numerical solution of Equation (101) (black) compared with the approximate solution (102) and (103) (green) versus (**a**) X_u and (**b**) q_0.

6.2.1. Values $q_0 \leq 1$

With Equations (10) and (102) we found for the peak time

$$\tau_E(q_0 \leq 1) = \frac{2.12[1 + 0.192(-\ln q_0)^{1.3}]}{1 + q_0}, \tag{104}$$

the peak redshift

$$z_E(q_0 \leq 1) = \left(\frac{2.533 \tilde{a}_0 (1 + q_0)}{h_{70} \left[1 + 0.192(-\ln q_0)^{1.3}\right]} \right)^{2/3} - 1 \tag{105}$$

and the peak SFR density

$$\Psi_{\max}(q_0 \leq 1) = 3.4986 \left(\frac{1 + 0.192(-\ln q_0)^{1.3}]}{1 + q_0} \right)^{5/3} \left[1 - \frac{0.618}{[1 + 0.192(-\ln q_0)^{1.3}]^2} \right], \tag{106}$$

so that

$$\begin{aligned} \psi_{\rm GSL}(z_E, q_0 \leq 1) &= 4.2205 \cdot 10^{-46}\, \tilde{a}_0^{1/3} h_{70}^{8/3} (1 + q_0)^2 \Psi_{\max} \\ &= 1.477 \cdot 10^{-45}\, \tilde{a}_0^{1/3} h_{70}^{8/3} (1 + q_0)^{1/3} \left(1 + 0.067(-\ln q_0)^{3/2} \right)^{5/3} \times \\ &\quad \left[1 - \frac{0.618}{[1 + 0.192(-\ln q_0)^{1.3}]^2} \right] \text{ kg s}^{-1} \text{ m}^{-3}, \end{aligned} \tag{107}$$

Equating Equation (105) with the observed peak redshift (94) readily yielded

$$\tilde{a}_0(q_0 \leq 1) = (2.05^{+1.11}_{-0.93}) \frac{h_{70} \left[1 + 0.192(-\ln q_0)^{1.3}\right]}{1 + q_0}, \tag{108}$$

while the equality of Equation (107) with the observed peak SFR density (93) leads to

$$\tilde{a}_0(q_0 \leq 1) = \frac{(0.0174^{+0.496}_{-0.010}) h_{70}^{-8} (1 + q_0)^{-1}}{[1 + 0.192(-\ln q_0)^{1.3}]^5 \, [1 - \frac{0.618}{[1 + 0.192(-\ln q_0)^{1.3}]^2}]^3}. \tag{109}$$

Note that for $q_0 = 1$ Equations (108) and (109) provide (Figure 6)

$$\tilde{a}_0(q_0 = 1) = (1.03^{+0.56}_{-0.47}) h_{70}, \tag{110a}$$

$$\tilde{a}_0(q_0 = 1) = (0.156^{+4.449}_{-0.089}) h_{70}^{-8}, \tag{110b}$$

which overlap very well.

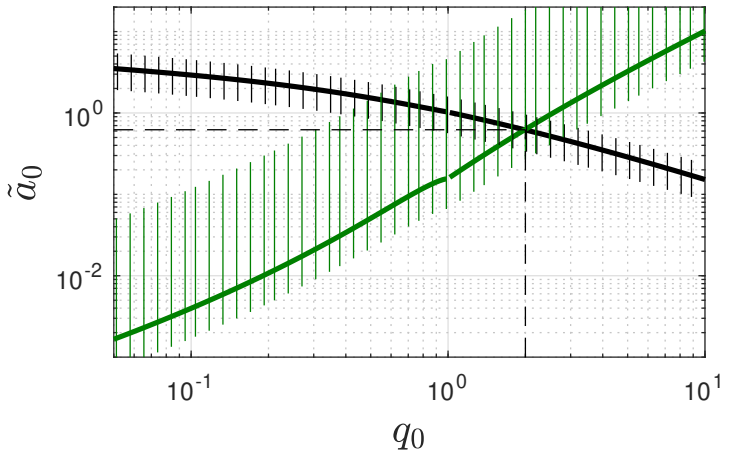

Figure 6. Observational constraint for GSL model parameters q_0 and $\tilde{a}_0$. Equations (108) and (115) (black) and Equations (109) and (116) (green) for $h_{70} = 1$. The vertical lines display the admissible ranges. The mean values cross at $q_0 \approx 2.0$ and $\tilde{a}_0 \approx 0.622$ (dashed). The green curve increases as $q_0^{3/2}$, while the black curve decreases as q_0^{-1} at $q_0 \gg 1$,in agreement with Equations (120).

6.2.2. Values $q_0 > 1$

With Equations (10) and (103) we obtained for the peak time

$$\tau_E(q_0 > 1) = \frac{5}{3}\frac{0.272 + q_0^{5/6}}{q_0^{5/6}(1+q_0)}, \tag{111}$$

the peak redshift

$$z_E(q_0 > 1) = \left(\frac{3.222\tilde{a}_0 q_0^{5/6}(1+q_0)}{h_{70}[0.272 + q_0^{5/6}]}\right)^{2/3}, -1 \tag{112}$$

and the peak SFR density

$$\Psi_{\rm max}(q_0 > 1) = 2.343\left[1 - \frac{q_0^{5/3}}{(0.272 + q_0^{5/6})^2}\right]\left(\frac{0.272 + q_0^{5/6}}{q_0^{5/6}(1+q_0)}\right)^{5/3}, \tag{113}$$

so that

$$\begin{aligned}\psi_{\rm GSL}(z_E, q_0 > 1) &= 4.2205\cdot 10^{-46}\,\tilde{a}_0^{1/3} h_{70}^{8/3}(1+q_0)^2\Psi_{\rm max}\\ &= 9.889\cdot 10^{-46}\,\tilde{a}_0^{1/3} h_{70}^{8/3}(1+q_0)^2\left(\frac{0.272 + q_0^{5/6}}{q_0^{5/6}(1+q_0)}\right)^{5/3}\times\\ &\quad\left[1 - \frac{q_0^{5/3}}{(0.272 + q_0^{5/6})^2}\right]\ {\rm kg\ s^{-1}\ m^{-3}}.\end{aligned} \tag{114}$$

Equating Equation (112) with the observed peak redshift (94) readily yielded

$$\tilde{a}_0(q_0 > 1) = (1.61^{+0.87}_{-0.74})\frac{h_{70}[0.272 + q_0^{5/6}]}{q_0^{5/6}(1+q_0)}, \tag{115}$$

while the equality of Equation (114) with the observed peak SFR density (93) lead to

$$\tilde{a}_0(q_0 > 1) = \frac{(0.0581^{+1.653}_{-0.0334})}{h_{70}^8(1+q_0)}\left[\frac{q_0^{5/6}}{0.272 + q_0^{5/6}}\right]^5\left[1 - \frac{q_0^{5/3}}{\left(0.272 + q_0^{5/6}\right)^2}\right]^{-3}. \tag{116}$$

All four expressions (108)–(109) and (115)–(116) for $\tilde{a}_0$ are displayed in Figure 6. As parameter values consistent with the observational constraints values we inferred from Figure 6

$$\tilde{a}_0 = 0.62^{+0.33}_{-0.29}, \quad q_0 = 2.0^{+1.2}_{-1.1}, \tag{117}$$

implying

$$a_0 = (0.62^{+0.33}_{-0.29})\cdot 10^{-17}\ {\rm Hz}, \tag{118a}$$

$$\beta_0 = a_0 q_0 = (1.24^{+1.80}_{-0.94})\cdot 10^{-17}\ {\rm Hz}. \tag{118b}$$

Consequently, the spontaneous and triggered star formation processes operate on time scales of $t_{\rm spont} \simeq 2.57^{+8.15}_{-1.52}$ Gyr and $t_{\rm trig} \simeq 5.13^{+4.52}_{-1.78}$ Gyr, respectively. The partly large error bars resulted from the large error bars on the observed SFR peak density (93).

Note that for $q_0 = 1$ the Equations (115) and (116) provide

$$\tilde{a}_0(q_0 = 1) = (1.02^{+0.55}_{-0.47})h_{70}, \tag{119a}$$

$$\tilde{a}_0(q_0 = 1) = (0.157^{+4.455}_{-0.090})h_{70}^{-8}, \tag{119b}$$

which agree perfectly with the earlier estimate (110). For very large values of $q_0 \gg 1$ Equations (115) and (116) yielded

$$\tilde{a}_0(q_0 \gg 1) = (1.61^{+0.87}_{-0.74})\frac{h_{70}}{q_0}, \tag{120a}$$

$$\tilde{a}_0(q_0 \gg 1) = (0.0581^{+1.653}_{-0.0334}) \cdot 6.21 q_0^{3/2} h_{70}^{-8}. \tag{120b}$$

In panels (a) and (c) of Figure 7 we compared the theoretical SFR density (96) with the observations collected by [38] where we varied freely the parameters $\tilde{a}_0$ and q_0. As can be seen, we obtained excellent agreement with the observations for the parameter choice $\tilde{a}_0 = 0.368$ and $q_0 = 2.67$. Both values are consistent with the range of parameter values (117) implied by the observational constraints discussed before. In panels (b) and (d) we show the corresponding fit to the observations of the integrated stellar density, to be discussed next. Here again, we found excellent agreement if additionally the parameter values $k_0 = 0.0039$ and $p_0 = 0.656$ so that $k_0 + p_0 = 0.66$ were chosen.

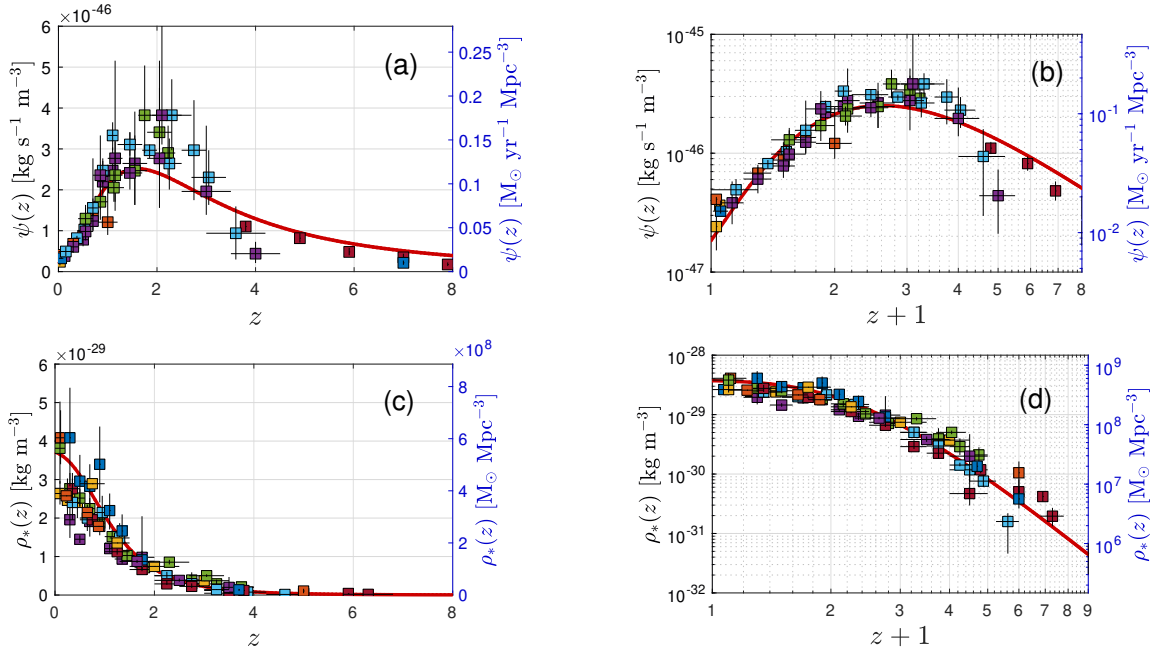

Figure 7. GSL model predictions. Fit to experimental data (symbols) from [38]. Our result (red solid line) for $\tilde{a}_0 = 0.368$, $q_0 = 2.97$, $k_0 = 0.0039$, $p_0 = 0.656$, i.e, $k_0 + p_0 \approx 0.66$. Shown are both (a,b) $\psi(z)$ and (**c**,**d**) $\rho_*(z)$ in (**a**,**c**) linear and (**b**,**d**) double-logarithmic representations.

6.3. Integrated Stellar Density

Likewise, the integrated stellar density (91) is given by

$$\begin{aligned}
\rho^*_{\rm GSL}(z) &= \frac{2B_1}{3\phi^{8/3}} \int_{\frac{\phi}{1101^{3/2}}}^{\frac{\phi}{(1+z)^{3/2}}} d\tau\, j(\tau) S(\tau) \tau^{5/3} \\
&\simeq \frac{B_1 q_0 (1+q_0)^3}{6\epsilon\phi^{8/3}} \int_0^{\frac{\phi}{(1+z)^{3/2}}} d\tau\, \frac{\tau^{5/3}}{\cosh^2 \frac{(1+q_0)(\tau-\tau_G)}{2}} \frac{e^{\epsilon\tau}-1}{1+e^{(1+q_0)(\tau-\tau_G)}} \\
&= \frac{B_1 q_0 (1+q_0)^3}{12\epsilon\phi^{8/3}} \int_0^{\frac{\phi}{(1+z)^{3/2}}} d\tau\, \frac{\tau^{5/3} e^{-\frac{(1+q_0)(\tau-\tau_G)}{2}}}{\cosh^3 \frac{(1+q_0)(\tau-\tau_G)}{2}} (e^{\epsilon\tau}-1) \\
&= \frac{2^{2/3} B_1 q_0^{1/2} (1+q_0)^{1/3}}{3\epsilon\phi^{8/3}} J\left(\frac{(1+q_0)\phi}{2(1+z)^{3/2}}\right),
\end{aligned} \tag{121}$$

where we used Equations (10), (78) and (86), substituted according to Equation (100), and introduced the integral

$$J(A) = \int_0^A dX\, \frac{X^{5/3} e^{-X} [e^{\frac{2\epsilon X}{1+q_0}} - 1]}{\cosh^3(X - X_u)}. \tag{122}$$

6.3.1. Asymptotics Of The Integral (122)

We investigated the asymptotic behavior of the integral (122) for small values of A with respect to unity, corresponding to large values of the redshift z. We obtained

$$\begin{aligned} J(A \ll 1) &\simeq \frac{2\epsilon}{1+q_0}\int_0^A dX\,\frac{X^{8/3}}{\cosh^3(X-X_u)} \\ &\simeq \frac{6\epsilon A^{11/3}}{11(1+q_0)\cosh^3(X_u)} = \frac{48\epsilon q_0^{3/2}A^{11/3}}{11(1+q_0)^4}. \end{aligned} \tag{123}$$

As $A(z) = (1+q_0)\phi/(2(1+z)^{3/2})$ the asymptotics (123) corresponds to

$$J(z \geq z_c) \simeq \frac{3\cdot 2^{1/3}\epsilon q_0^{3/2}\phi^{11/3}}{11(1+q_0)^{1/3}(1+z)^{11/2}}, \tag{124}$$

with the characteristic redshift

$$z_c = \left[\frac{1+q_0)\phi}{2}\right]^{2/3} - 1 = 1.93\left[\frac{(1+q_0)\tilde{a}_0}{h_{70}}\right]^{2/3} - 1 \tag{125}$$

of order unity. We then obtained for Equation (121) in this limit

$$\rho^*_{\rm GSL}(z \geq z_c) \simeq \frac{2B_1 q_0^2\phi}{11(1+z)^{11/2}} = \frac{2.19\cdot 10^{-26}\,q_0^2\tilde{a}_0^3}{h_{70}(1+z)^{11/2}}\ \text{kg m}^{-3}. \tag{126}$$

This asymptotic is significantly steeper than the $(1+z)^{-4}$ behavior obtained in part I for neglected triggered star formation. In the alternative case of large arguments $A \gg 1$ the integral (122) was approximated in Appendix D as

$$\begin{aligned} J(A \gg 1) &\simeq \frac{3}{2\cosh^3(X_u)}\left[\left(\frac{4}{3}+\frac{2(k_0+p_0)}{1+q_0}\right)^{-8/3} - 0.04\right] \\ &= \frac{12q_0^{3/2}}{(1+q_0)^3}\left[\left(\frac{4}{3}+\frac{2(k_0+p_0)}{1+q_0}\right)^{-8/3} - 0.04\right]. \end{aligned} \tag{127}$$

6.3.2. Present-Day Integrated Stellar Density

For the present-day integrated stellar density at redshift $z = 0$ we note that with our earlier parameter estimates (117) $A(z=0) = 2.69(1+q_0)\tilde{a}_0 h_{70}^{-1} \simeq 4.99$ is large compared to unity so that we used the approximation (127) providing for Equation (121)

$$\begin{aligned} \rho^*_{\rm GSL}(0) &\simeq \frac{2^{8/3}B_1 q_0^2}{\epsilon(1+q_0)^{8/3}\phi^{8/3}}\left[\left(\frac{4}{3}+\frac{2(k_0+p_0)}{1+q_0}\right)^{-8/3} - 0.04\right] \\ &= \frac{1.61\cdot 10^{-27}\,h_{70}^{8/3}q_0^2}{\tilde{a}_0^{2/3}\epsilon(1+q_0)^{8/3}}\left[\left(\frac{4}{3}+\frac{2(k_0+p_0)}{1+q_0}\right)^{-8/3} - 0.04\right]\ \text{kg m}^{-3}. \end{aligned} \tag{128}$$

Equating the constraint (95) with Equation (128) then yielded

$$\tilde{a}_0 = \frac{(276^{+140}_{-94})\,h_{70}^4 q_0^3}{(1+q_0-p_0-k_0)^{3/2}(1+q_0)^4}\left[\left(\frac{4}{3}+\frac{2(k_0+p_0)}{1+q_0}\right)^{-8/3} - 0.04\right]^{3/2}. \tag{129}$$

In contrast with the earlier constraints (108) and (109) the constraint (129) depends on the sum $p_0 + k_0$ of the additional ratios k_0 and p_0 characterizing the strength of stellar evolution and feedback, respectively. For $\tilde{a}_0$ and q_0 from Equation (117), Equation (129) yielded $k_0 + p_0 = 0.585^{+0.574}_{-0.317}$ in excellent agreement with the numerical fit in Figure 8.

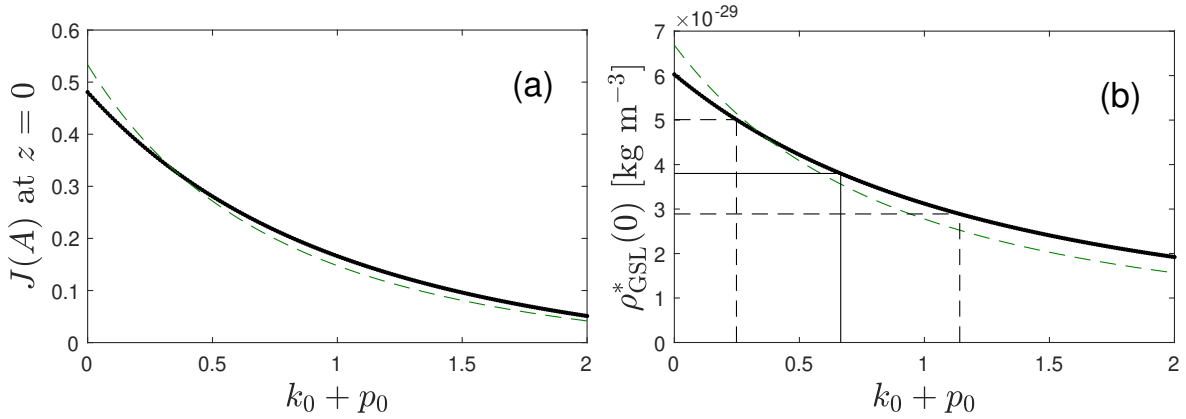

Figure 8. Observational constraint for GSL model parameter $k_0 + p_0$. (**a**) Numerical $J(A)$ from Equation (122) for $z = 0$ and (**b**) $\rho^*_{\rm GSL}(0)$ using this $J(A)$ according to Equation (121), both versus $k_0 + p_0$ for $q_0 = 2$, $\tilde{a}_0 = 0.62$ and $h_{70} = 1$. The $\rho^*_{\rm GSL}(0)$ matches the value $3.80 \cdot 10^{-29}$ (95) at $k_0 + p_0 \approx 0.66$ (vertical solid line), in perfect agreement with our best fit to the experimental data (Figure 7). Taking into account experimental errors, the range of admissible $k_0 + p_0$ values is $k_0 + p_0 \in [0.25, 1.14]$ (dashed vertical lines). The green dashed lines in panels (**a**) and (**b**) are the analytical expressions (127) and (128).

7. Redshift Dependency Of The Gas And Stellar Fractions And Future Of The Baryonic Universe

Here, the best fit parameter values for the three ratios q_0, p_0 and k_0 and the triggered star formation rate a_0 from the last section were used to determine the present-day ($z = 0$) gas and stellar fractions. The three panels in Figure 9 display the resulting reduced time and redshift dependencies of the fractions using Equations (74), (78), and (88). The error bars according to Equations (117) and $k_0 + p_0 \in [0.25, 1.14]$ from the fits in Figure 8 are represented as gray lines, whose darkness moderately increases with their probability, assuming Gaussian distributed $\tilde{a}_0$ and q_0.

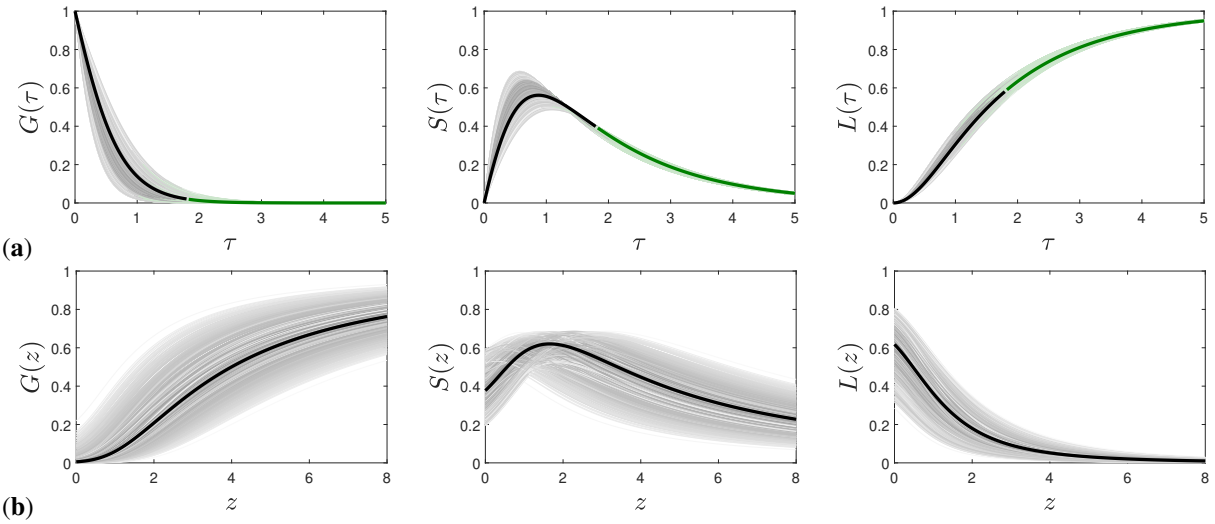

Figure 9. GSL model predictions. G, S, and L for the parameters $\tilde{a}_0 = 0.62$, $q_0 = 2$, $k_0 = 0.0039$, $p_0 = 0.656$. The lines in (**a**) are $G(\tau)$ (74), $S(\tau)$ (78), and $L(\tau) = 1 - G(\tau) - S(\tau)$ (88) obtained using the approximation Equation (42) for $U(\tau) = -\ln[Y(\tau)]$ with coefficients c_1, α_1, and α_2 given by Equation (73). Lines in (**b**) are $G(z) = G(\tau(z))$ etc. with $\tau(z)$ from Equation (10). Error bars from Equation (117). They are represented as gray lines, whose darkness moderately increases with their probability, assuming Gaussian distributed $\tilde{a}_0$ and q_0. The future corresponding to $\tau \geq \tau(0) = 5.37\tilde{a}_0\sqrt{3} \approx 1.83$, is colored green. Note that the error bars in panel (**a**) are smaller than in panel (**b**) because the fractions (74), (78), (88) as a function of reduced time only depend on the parameter q_0 but not on the parameter $\tilde{a}_0$.

These panels not only show the history of the cosmological gas and stellar fractions as a function of redshift z in panel (b), but also their future evolution as a function of the reduced time τ in panel (a). Note that the present-day epoch, depending on $\tilde{a}_0$ corresponds to about $\tau(z = 0) = 1.83$, so that the future starts beyond this time. In panel (a) of Figure 9 we marked the future epochs in green colour. It is clear, however, that ultimately at $\tau = \infty$ the stationary state with values

$$G_\infty = 0, \qquad \frac{G_\infty}{1-G_\infty} = 0, \qquad \frac{G_\infty}{S_\infty} = 0 \tag{130}$$

is attained.

Next, we considered the present-day ($z = 0$) gas and stellar fractions. As present-day quantities have to be calculated, we used the modification $\zeta(0)$ in Equations (10)–(12) for $\tau(z = 0)$).

7.1. Present-Day Gas Fraction

According to Equation (74) the Equation (10) predicts for the present-day gas fraction

$$G(z=0) \quad = \quad \frac{1+q_0}{1+q_0 e^{(1+q_0)\tau(0)}} = \frac{1+q_0}{1+q_0 e^{2.94(1+q_0)\tilde{a}_0 h_{70}^{-1}}}, \tag{131}$$

which can be contrasted with the observed Milky Way gas fraction of ≈ 0.1 ([45]). With the parameters (117) we obtained for $h_{70} = 1$

$$G(z=0) = 0.00631^{+0.278}_{-0.00629} \tag{132}$$

Within the large error bars, this prediction is consistent with the observed gas fraction of about 10 percent. The gas fraction (132) also provided the present-day interstellar gas mass to total (including locked-in matter) stellar mass.

$$\frac{G(z=0)}{S(z=0)+L(z=0)} \quad = \quad \frac{G(z=0)}{1-G(z=0)} = 0.00635 \tag{133}$$

for the nominal parameter values $q_0 = 2$ and $\tilde{a}_0 = 0.62$.

7.2. Stellar Fractions

Likewise, from Equation (78) we obtained

$$S(z=0) = \frac{q_0[e^{\epsilon\tau(0)}-1]G(z=0)}{\epsilon} = \frac{q_0[e^{2.94\epsilon\tilde{a}_0 h_{70}^{-1}}-1]G(z=0)}{\epsilon}. \tag{134}$$

For the nominal values $q_0 = 2$, $\tilde{a}_0 = 0.62$, $p_0 + k_0 = 0.66$, so that $\epsilon = 2.34$, we found

$$S(z=0) = 0.379^{+0.224}_{-0.191}, \qquad L(z=0) = 0.615^{+0.197}_{-0.378} \tag{135}$$

for the ratio of the present-day interstellar gas mass to luminous stellar mass

$$\frac{G(z=0)}{S(z=0)} \quad = \quad 0.01665^{+0.5627}_{-0.01665}. \tag{136}$$

The last ratio could be compared with the observed gas/stellar mass fraction in $z \sim 0$ galaxies ([46,47]) as the stellar component has been obtained from large galaxy surveys in the optical/infrared band, where locked-in stellar matter contributes negligibly small emission. The observations reveal ratios as a function of stellar mass in the range $[0.01, 0.7]$. The estimate (136) is consistent with the observations but excludes the large positive error bar.

The estimates (135) indicated that at the present time the majority of the baryons (more than 72 percent) resides in the form of stellar matter with $61.5^{+19.7}_{-37.8}$ percent in locked-in stellar matter (white dwarfs, neutron stars and black holes) and $37.9^{+22.4}_{.19.1}$ percent in the form of luminous main-sequence stars. These estimates had to be contrasted with expectations from stellar evolution models. In these models, for a reasonable choice of the initial mass function (see for example [48, 49]), a stellar population of approximately 13 Gyr has only returned about $R \sim 40\%$ of its originally formed mass to the interstellar medium (ISM), with $(1 - R) \sim 60\%$ remaining as surviving stars or remnants. Of that $\sim 60\%$, only around $\sim 25\%$ consists of remnants (white dwarfs, black holes, and neutron stars)—see Section 2.1.2 of the review by [50]. Within their uncertainties, the estimates (135) are consistent with the stellar evolution model calculations, which have their own uncertainties.

7.3. Remarks

We can conclude this section with two important remarks:

(1) It had not escaped from our attention that we can only constrain analytically the sum of the two parameters $p_0 + k_0$ from the comparison of the integrated stellar light as well as the stellar fractions. This is a drawback

of our approximation of the exact Equation (46): without the function $R(\tau)$, this equation indeed only involves the sum $p_0 + k_0$. Therefore, any dependence on the individual values of p_0 and k_0 only stems from the function $R(\tau)$ calculated in Equation (54). However, with the adopted relation (56) involving only $R(\infty)$, which with the choice (57) then also depends only on the sum $p_0 + k_0$, any dependency on the individual values of p_0 und k_0 was not possible anymore. This could be proven by comparing the exact numerical solutions of $S(\tau)$ for the two cases $(k_0 = 0.2, p_0 = 0.5)$ and $(k_0 = 0.5, p_0 = 0.2)$ shown in Figure 10. As in both cases the sum $p_0 + k_0 = 0.7$ is the same, our approximation yielded the same time dependence of $S(\tau)$, whereas the exact numerically calculated variations were different.

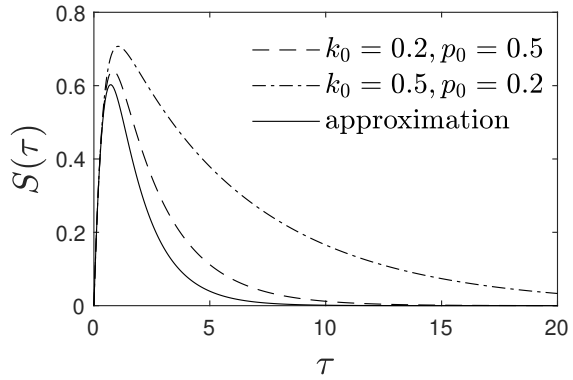

Figure 10. Feature of the approximate GSL solution. $S(\tau)$ versus τ according to Equations (73), (75), and (78) for $q_0 = 2$ and two cases for which the sum $k_0 + p_0$ is identical. The analytical approximation yields just one curve (solid), while the numerical solutions (dashed and dot-dashed) of the GSL-equation differ.

(2) The second remark concerns the value of the Hubble constant. In contrast to part I, we here were in accord with all observational constraints for the standard value $h_{70} = 1$ of the Hubble constant and did not have to speculate on substantially smaller values of the Hubble constant as in part I.

8. Summary and Conclusions

In this work, we extended the analysis of the compartmental description of the temporal evolution of the baryonic matter in stars and interstellar gas, pioneered in part I, by the inclusion of the triggered star formation process. As in part I the introduction of gaseous and stellar fractions of the total baryonic matter as the basic dynamical variables is advantageous because it allows to apply the analysis to a variety of astrophysical systems. The competition of triggered and spontaneous star formation, stellar feedback, and stellar evolution is theoretically investigated with analytical and numerical solutions of the nonlinear dynamical GSL equations for the interstellar and intergalactic gas fraction $G(t)$, the luminous stellar matter fraction $S(t)$, and the locked-in matter fraction $L(t)$.

By introducing the dimensionless reduced time variable τ (8) for arbitrarily but given time-dependent triggered SFR coefficient $a(t)$, as well as the dimensionless ratios $q(t) = \beta(t)/a(t)$, $k(t) = b(t)/a(t)$ and $p(t) = c(t)/a(t)$, the derived exact solutions of the GSL equations for stationary ratios q_0, k_0 and p_0 hold for stationary rates as well as for the case of the same time-dependency of all rates. The accuracy of the analytical solutions is confirmed by comparison with the exact numerical solutions of the GSL equations. Once again, of particular interest is the understanding of the cosmic star formation history, the present-day gas and stellar fraction, and their ultimate future fate with compartmental models. For a flat ΛCDM Friedmann cosmology, the relationship between the reduced time variable $\tau(z)$ and the cosmological redshift z is used to calculate the effect of redshift on the cosmological star formation rate, the integrated stellar density, and the present-day gas and stellar fractions. In contrast to part I, the cosmological star formation rate now has two contributions from the spontaneous and triggered formation processes.

The inclusion of the nonlinear triggered star formation process enormously complicated the derivation of analytical solutions. Exact solutions of the GSL equations were derived in Section 3 for the case of negligible stellar evolution and served an important dual purpose, namely to test the accuracy of the numerical code solving the GSL equations as well as to compare with the analytical approximations derived in the most general case in the respective limit of negligible stellar evolution. For the most general case of all four competing processes operating simultaneously with stationary ratios, we reduced the coupled dynamical GSL equations in Section 3 to one exact nonlinear integro-differential equation (see Equations (A35) and (46)) determining the time evolution for $U(\tau) = \int_0^\tau d\tau' G(\tau') - (p_0 + k_0)\tau$ from which the gas and stellar fractions can be determined. Approximate analytical solutions were derived in Section 5 for the case of small times $\tau \leq p_0^{-1}$ and for general times for positive values of the ratio p_0 characterizing the stellar evolution process. The small times solution in the case of negligible

stellar evolution ($p_0 = 0$) holds at all times and agrees exactly with the earlier derived exact solutions in this special case in Section 5. The accuracy of the approximate solution in the general case of finite p_0 is demonstrated by comparison with the numerical solutions. Most noteworthy, for small enough rates of stellar feedback determining the ratio k_0 the derived gas fraction and the formation rate (86) of new stars as a function of the reduced time τ are solely determined by the ratio q_0 of spontaneous to triggered star formation, whereas the remaining two ratios k_0 and p_0 exhibit themselves in the temporal evolution of the stellar fractions $S(\tau)$ and $L(\tau)$. This is in accord with the starting reduced GSL equations Equations (14b) and (17) that do not directly involve the ratio p_0.

The near independence of the formation rate (86) of new stars as a function of the reduced time τ significantly facilitates the calculation of the cosmological SFR as a function of redshift (Section 6), which, for an adopted constant triggered star formation rate a_0, depends only on the two parameters a_0 and $q_0 = \beta_0/a_0$. The comparison with the observed SFR provides as best fit values $a_0 = 0.368$ and $q_0 = 2.97$, $k_0 = 0.0039$ and $p_0 = 0.656$ so that $p_0 + k_0 = 0.66$. Due to the partly large uncertainties in the observed peak SFR rate, the error bars on these parameters are $\tilde{a}_0 = 0.62^{+0.39}_{-0.29}$, $q_0 = 2.0^{+1.2}_{-1.1}$ and $k_0 + p_0 = 0.585^{+0.574}_{-0.317}$. In Section 7 We calculated the resulting reduced and redshift dependencies of the three gas and stellar fractions. These not only show the history of the cosmological gas and stellar fractions as a function of redshift z, but also predict their future evolution as a function of the reduced time τ. Within the error bars, the calculated present day gas and stellar fractions are consistent with the observed Milky Way gas fraction of 0.1 as well as the observed gas/stellar mass fraction in $z \sim 0$ galaxies. They also agree reasonably well with expectations from stellar evolution models.

Our analysis applies to stationary rates but can also be applied to *any* time-dependent star formation rate $a(t)$, provided the additional rates $b(t), \beta(t)$ and $c(t)$ have exactly the same time variation as $a(t)$. This is the advantage when introducing the reduced time scale (8). As there is no obvious other choice for the time variation of $a(t)$, we adopted the simplest possibility (Occam's razor), a stationary star formation rate. Because of the good agreement with the observations at this point, we see no strong reason to investigate more complicated time-dependent rates $a(t)$. The latter would modify the reduced time redshift relation in Appendix A. It also would severely complicate the connection to the work in part I, as Equation (9) then no longer holds. Of course, it is possible that other time-dependent star formation rates also provide acceptable fits to the observations.

A most important result of this investigation is that the inclusion of the triggered star formation process explains the observed cosmological star formation rate and the integrated stellar density as well as the present-day gas and stellar fractions much better than the simplified GSL-model of part I, ignoring triggered star formation. The best-fit parameter values to the observations indicate that the spontaneous and triggered star formation processes dominate the dynamical evolution of baryonic matter in the universe, as indicated by the best-fit value of the sum of ratios $p_0 + k_0$ being significantly smaller than unity. For an adopted constant triggered star formation rate a_0, the spontaneous and triggered star formation processes operate on time scales of $t_{\rm spont} \simeq 2.57^{+8.15}_{-1.52}$ Gyr and $t_{\rm trig} \simeq 5.13^{+4.52}_{-1.78}$ Gyr, respectively. Interestingly, the spontaneous formation process is about twice as effective than the triggered formation process.

After the non-perfect agreement of the simplified GSL-model with only the spontaneous star formation process investigated in part I, we can now conclude that the inclusion of the triggered star formation process has improved the situation significantly. This generalized GSL-model is consistent with all observational constraints from the cosmological star formation history and the corresponding integrated stellar density. The model provides excellent fits to the observed redshift dependencies of the star formation rate and the integrated stellar density. Moreover, it explains the observed present-day gas and stellar fractions in the universe, and it makes predictions on the future evolution of these fractions in the universe. The presented analysis of the GSL compartmental model has led to new and original insights on the cosmological baryonic matter cycle in the universe.

Author Contributions

R.S.: conceptualization, methodology, formal analysis, writing-reviewing and editing; M.K.: methodology, formal analysis, software, writing-reviewing and editing, visualization. All authors have read and agreed to the published version of the manuscript.

Informed Consent Statement

Not applicable.

Data Availability Statement

All data are enclosed with this publication.

Acknowledgments

R.S. gratefully acknowledges the institutional support by the Astrophysics Group headed by Wolfgang Duschl and Sebastian Wolf at the Institut für Theoretische Physik und Astrophysik of the Christian-Albrechts-Universität in Kiel, Germany.

Conflicts of Interest

The authors declare no conflict of interest.

Use of AI and AI-Assisted Technologies

No AI tools were utilized for this paper.

Appendix A. Reduced Time Redshift Relation

With Equation (9) we obtained for the relation between the reduced time τ and the redshift z in a flat ΛCDM Friedmann cosmology

$$\tau(z) = \frac{2a_0[0.424+f(\tau)]}{3\sqrt{1-\Omega_0}H_0} = \frac{3.513\tilde{a}_0[0.424+f(\tau)]}{h_{70}}\ \mathrm{s} \tag{A1}$$

with

$$f(\tau) = \ln\frac{1+\sqrt{1+\frac{\Omega_0}{1-\Omega_0}(1+z)^3}}{(1+z)^{\frac{3}{2}}} = \ln\frac{1+\sqrt{1+\frac{3}{7}(1+z)^3}}{(1+z)^{\frac{3}{2}}}, \tag{A2}$$

where $\Omega_m = \Omega_0 = 0.3$ and $H_0 = 70h_{70}$ km s^{-1}Mpc^{-1} $= 2.268\cdot 10^{-18}h_{70}$ s^{-1} according to Equation (I-39) for a constant triggered star formation rate $a(t) = a_0 = 10^{-17}\tilde{a}_0$. Equations (A1) and (A2) imply

$$\frac{df(\tau)}{d\tau} = -\frac{3}{2(1+z)\sqrt{1+\frac{\Omega_0}{1-\Omega_0}(1+z)^3}}, \tag{A3}$$

and thus

$$\frac{d\tau}{dz} = -\frac{a_0}{H_0\sqrt{\Omega_0}\sqrt{(1+z)^3+\frac{1-\Omega_0}{\Omega_0}}}. \tag{A4}$$

For redshift values

$$z > \left(\frac{1-\Omega_0}{\Omega_0}\right)^{1/3} - 1 = 0.326 \tag{A5}$$

we approximated, following part I, the Equation (A4) as

$$\frac{d\tau}{dz} \simeq -\frac{a_0}{\sqrt{\Omega_0}H_0(1+z)^{5/2}}, \tag{A6}$$

corresponding to

$$\tau(z) \simeq a_0\tau_f(1+z)^{-3/2}, \tag{A7}$$

$$\tau_f = \frac{2}{3H_0\sqrt{\Omega_0}} = \frac{5.37\cdot 10^{17}}{h_{70}}\ \mathrm{s}. \tag{A8}$$

Obviously, the approximations (A6)–(A8) are excellent for redshift values significantly greater than 0.326, but not accurate enough for redshift values close to zero. Here we used the improved approximation

$$\tau_f = \frac{2\zeta}{3H_0\sqrt{\Omega_0}} = 2.94\cdot 10^{17}\,h_{70}^{-1}\ \mathrm{s}, \tag{A9}$$

where the factor

$$\zeta = \sqrt{3/10} = 0.548 \tag{A10}$$

ensured that $d\tau/dz$ is captured exactly at $z = 0$. Note that the exact value from Equation (A4) is $d\tau/dz|_{z=0} = -a_0/H_0\sqrt{10\Omega_0/3}$, where the value from the approximation (A6) is given by $-a_0/H_0\sqrt{\Omega_0}$.

Accordingly, the reduced time redshift relation (A1) for all values of z is well approximated by Equations (10)–(12), that is

$$\tau(z) \simeq \frac{\phi}{(1+z)^{3/2}}, \qquad \phi = \frac{5.37\tilde{a}_0\zeta(z)}{h_{70}}, \tag{A11}$$

$$\zeta(z) = \frac{(1+z)^{3/2}}{\sqrt{\frac{7}{3}+(1+z)^3}}, \tag{A12}$$

$$\zeta(0) = \sqrt{\frac{3}{10}} = 0.548. \tag{A13}$$

Appendix B. Reduction of the Full GSL-Equations

Appendix B.1. Reduction

For the full GSL-model including stellar evolution $p_0 > 0$ we first reduced Equations (20) further. Equation (20a) readily yielded

$$N(\tau) = -\frac{\frac{dM(\tau)}{d\tau} + q_0 k_0}{M(\tau)}, \tag{A14}$$

and Equation (20b) could be written as

$$p_0 = M(\tau) + \frac{q_0(k_0+p_0)}{N(\tau)} - \frac{d\ln N(\tau)}{d\tau}. \tag{A15}$$

Substituting

$$N(\tau) = q_0(k_0+p_0)X(\tau) \tag{A16}$$

the Equation (A15) reads

$$p_0 - M(\tau) = \frac{1}{X(\tau)} - \frac{d\ln X(\tau)}{d\tau} = \frac{1}{X(\tau)}\left[1 - \frac{dX(\tau)}{d\tau}\right], \tag{A17}$$

or equivalently,

$$\frac{dX(\tau)}{d\tau} + [p_0 - M(\tau)]X(\tau) = 1. \tag{A18}$$

This last Equation (A18) was readily solved by

$$X(\tau) = \left[c_0 + \int_0^\tau dx\, e^{p_0 x - \int_0^x d\tau' M(\tau')}\right] e^{-p_0\tau + \int_0^\tau d\tau' M(\tau')} \tag{A19}$$

with the integration constant $c_0 = X(0)$. The solution (A19) implied

$$N(\tau) = q_0(k_0+p_0)\left[c_0 + \int_0^\tau dx\, e^{p_0 x - \int_0^x d\tau' M(\tau')}\right] e^{-p_0\tau + \int_0^\tau d\tau' M(\tau')}. \tag{A20}$$

The initial value $N(\tau = 0) = q_0$ then provided $c_0 = 1/(k_0+p_0)$, so that

$$\begin{aligned} S(\tau) &= N(\tau) - q_0 \\ &= q_0\left[1 + (k_0+p_0)\int_0^\tau dx\, e^{-U(x)}\right] e^{U(\tau)} - q_0, \end{aligned} \tag{A21}$$

where we introduced

$$U(\tau) = \int_0^\tau d\tau' M(\tau') - p_0\tau, \tag{A22}$$

implying

$$\begin{aligned} M(\tau) &= G(\tau) - k_0 = \frac{dU(\tau)}{d\tau} + p_0, \\ \frac{dM(\tau)}{d\tau} &= \frac{dG(\tau)}{d\tau} = \frac{d^2U(\tau)}{d\tau^2}, \end{aligned} \tag{A23}$$

with

$$\begin{aligned} U(0) &= 0, \qquad U''(0) = G'(0) = -q_0, \\ U'(0) &= G(0) - k_0 - p_0 = 1 - k_0 - p_0. \end{aligned} \tag{A24}$$

Inserting Equations (A21) and (A23) yielded for Equation (A14)

$$-q_0 k_0 = \frac{d^2U}{d\tau^2} + q_0 \left[\frac{dU(\tau)}{d\tau} + p_0\right] e^{U(\tau)} \left[1 + (k_0 + p_0) \int_0^\tau dx\, e^{-U(x)}\right]. \tag{A25}$$

With

$$\frac{dU(\tau)}{d\tau} e^{U(\tau)} = \frac{d}{d\tau} e^{U(\tau)}, \tag{A26}$$

and

$$\frac{de^{U(\tau)}}{d\tau} \int_0^\tau dx\, e^{-U(x)} = \frac{d}{d\tau}\left[e^{U(\tau)} \int_0^\tau dx\, e^{-U(x)}\right] - 1 \tag{A27}$$

the Equation (A25) could be further reduced to

$$\begin{aligned} &\frac{d}{d\tau}\left[\frac{dU(\tau)}{d\tau} + q_0 e^{U(\tau)} \left(1 + (k_0 + p_0) \int_0^\tau dx\, e^{-U(x)}\right)\right] \\ &\quad = q_0 p_0 \left[1 - e^{U(\tau)} \left(1 + (k_0 + p_0) \int_0^\tau dx\, e^{-U(x)}\right)\right]. \end{aligned} \tag{A28}$$

Setting

$$Z(\tau) = \frac{dU(\tau)}{d\tau} + q_0 e^{U(\tau)} \left(1 + (k_0 + p_0) \int_0^\tau dx\, e^{-U(x)}\right), \tag{A29}$$

Equation (A28) reads

$$q_0 p_0 + p_0 \frac{dU(\tau)}{d\tau} = \frac{dZ(\tau)}{d\tau} + p_0 Z(\tau) = e^{-p_0\tau} \frac{d}{d\tau}[Z(\tau) e^{p_0\tau}]. \tag{A30}$$

With the initial conditions $U(0) = 0$ and

$$Z(0) = U'(0) + q_0 = 1 + q_0 - k_0 - p_0 = \epsilon, \tag{A31}$$

Equation (A30) integrated to

$$Z(\tau) = q_0 + (\epsilon - q_0) e^{-p_0\tau} + p_0 e^{-p_0\tau} \int_0^\tau dx\, e^{p_0 x} \frac{dU(x)}{dx}. \tag{A32}$$

Inserting Equation (A32) then provided for Equation (A29)

$$\begin{aligned} \frac{dU(\tau)}{d\tau} &+ q_0 e^{U(\tau)} \left(1 + (k_0 + p_0) \int_0^\tau dx\, e^{-U(x)}\right) \\ &= q_0 + (\epsilon - q_0) e^{-p_0\tau} + p_0 e^{-p_0\tau} \int_0^\tau dx e^{p_0 x} \frac{dU(x)}{dx}. \end{aligned} \tag{A33}$$

We note that with $U'(0) = 1 - (k_0 + p_0) = \epsilon - q_0$

$$(\epsilon - q_0) e^{-p_0\tau} = \epsilon - q_0 - p_0 e^{-p_0\tau} \int_0^\tau dx e^{p_0 x} U'(0), \tag{A34}$$

so that Equation (A33) could be written as

$$\begin{aligned} \frac{dU(\tau)}{d\tau} &+ q_0 e^{U(\tau)} \left(1 + (k_0 + p_0) \int_0^\tau dx\, e^{-U(x)}\right) \\ &= \epsilon + p_0 e^{-p_0 \tau} \int_0^\tau dx\, e^{p_0 x} \left[\frac{dU(x)}{dx} - \left(\frac{dU}{dx}\right)_{x=0}\right]. \end{aligned} \tag{A35}$$

Equations (A25), (A28) and (A35) represent exact determining nonlinear integro-differential equations for the function $U(\tau)$ defined in Equation (A22). In the Section 5 we solved Equation (A35) approximately.

Appendix B.2. Final Values

As

$$G(\tau) = U'(\tau) + k_0 + p_0, \quad G_\infty = U'(\infty) + k_0 + p_0 \tag{A36}$$

we inspected the limiting value of $U(\infty)$ and $U'(\infty)$. We considered first the limiting values of Equations (A29) and (A32) using L'Hospital's rule for

$$\lim_{\tau\to\infty} \frac{(k_0 + p_0) \int_0^\tau dx\, e^{-U(x)}}{e^{-U(\tau)}} = -\frac{k_0 + p_0}{U'(\infty)}, \tag{A37}$$

$$\lim_{\tau\to\infty} \frac{p_0 \int_0^\tau dx\, e^{p_0 x} U'(x)}{e^{p_0 \tau}} = U'(\infty), \tag{A38}$$

so that Equation (A32) provided

$$Z(\infty) = q_0 + U'(\infty), \tag{A39}$$

whereas Equation (A29) yielded

$$Z(\infty) = -\frac{q_0(k_0 + p_0)}{U'(\infty)} + U'(\infty) + q_0 e^{U(\infty)}. \tag{A40}$$

The last two Equations (A39) and (A40) only agree if

$$e^{U(\infty)} = 1 + \frac{k_0 + p_0}{U'(\infty)}. \tag{A41}$$

Likewise, the limit (A37) yielded for Equation (A21)

$$S_\infty = q_0 \left[e^{U(\infty)} - 1 - \frac{k_0 + p_0}{U'(\infty)}\right] = 0, \tag{A42}$$

if we inserted Equation (A41). The additional requirement $U(\infty) = -\infty$ so that $e^{U(\infty)} = 0$ then demanded according to Equation (A41) that

$$U'(\infty) = -(k_0 + p_0), \tag{A43}$$

implying

$$G_\infty = 0, \qquad L(\infty) = 1 - G_\infty - S_\infty = 1. \tag{A44}$$

thus reproducing correctly the earlier noted stationarity property (18).

Appendix C. Consistency Check: Comparison With Earlier Results For Vanishing Stellar Evolution $p_0 = 0$

In the case of vanishing stellar evolution ($p_0 = 0$) considered before in Section 3 the solution (69) holds for all times. Moreover, in this case the un-approximated full Equation (A35) agrees exactly with the approximated Equation (61). Therefore the derived solution (69) had to agree with the solution (32). We checked this consistency noting that for $p_0 = 0$ one has according to Equation (A31), $\epsilon = 1 + q_0 - k_0 = \epsilon_0$, so that according to Equation (63)

$$\omega = \sqrt{(1 + q_0 + k_0)^2 - 4k_0} = \sqrt{\chi_0^2 - 4k_0} = \omega_0 \tag{A45}$$

in terms of the quantities defined in Equation (29) in Section 3. Then Equation (69) reduced to

$$G(\tau) = G_\infty^0 + \frac{\omega_0}{1 + \alpha_0 e^{\omega\tau}}, \tag{A46}$$

with

$$G_\infty^0 = k_0 + \frac{\epsilon_0 - \omega_0}{2} = \frac{\chi_0 - \omega_0}{2}, \tag{A47}$$

and

$$\alpha_0 = \frac{\omega_0 - \epsilon_0 + 2q_0}{\omega_0 + \epsilon_0 - 2q_0} = \frac{\omega_0 + q_0 + k_0 - 1}{\omega_0 + 1 - q_0 - k_0} = \frac{\omega_0}{1 - G_\infty^0} - 1, \tag{A48}$$

as

$$\frac{\omega_0}{1 - G_\infty^0} - 1 = \frac{\omega_0 - 1 + G_\infty^0}{1 - G_\infty^0} = \frac{2\omega_0 - 1 + \chi_0 - \omega_0}{2 + \omega_0 - \chi_0} = \frac{\omega_0 + q_0 + k_0 - 1}{\omega_0 + 1 - q_0 - k_0}. \tag{A49}$$

Consequently, Equation (A46) agrees exactly with the earlier solution (32). This completes the proof of consistency.

Appendix D. Present-Day Integrated Stellar Density

In Equation (122) we introduced this integral

$$J(A) \quad = \quad \int_0^A \frac{X^{5/3} e^{-X} [e^{2cX} - 1] dX}{\cosh^3(X - X_u)}, \quad c = 1 - \frac{k_0 + p_0}{1 + q_0}. \tag{A50}$$

We were interested in an approximation to this integral in the vicinity of $q_0 \approx 2$ and $A \approx 5$. The integrand basically vanishes for $X \geq 5$ for any $k_0 + p_0 \in [0, 1]$, so that

$$J(A) \simeq J(\infty) = \int_0^\infty dX \, \frac{X^\mu e^{-X} [e^{2cX} - 1]}{\cosh^3(X - X_u)}. \tag{A51}$$

The denominator of the integrand is a function that increases near-exponentially with increasing X. We thus wrote

$$\frac{1}{\cosh^3(X - X_u)} \simeq a e^{-bX} \tag{A52}$$

with coefficients a and b that we determined by matching the left and right hand sides in Equation (A52) at $X = 0$ and $X = \sqrt{3}$. This gave $a = 1/\cosh^3(X_u)$ and

$$b = \frac{\ln[\cosh^3(\sqrt{3} - X_u)] - \ln[\cosh^3(X_u)]}{\sqrt{3}}. \tag{A53}$$

For $q_0 \approx 2$, $X_u \approx -0.35$ and $b \approx 7/3$. Using this approximation

$$\begin{aligned} J(A) \quad &\simeq \quad \frac{1}{\cosh^3(X_u)} \int_0^\infty dX \, X^\mu e^{-\frac{10X}{3}} [e^{2cX} - 1] \\ &= \quad \frac{\Gamma(8/3)}{\cosh^3(X_u)} \left[\frac{1}{\left(\frac{10}{3} - 2c\right)^{8/3}} - \frac{9}{100} \left(\frac{3}{10}\right)^{2/3} \right] \\ &\simeq \quad \frac{3}{2\cosh^3(X_u)} \left[\left(\frac{4}{3} + \frac{2(k_0 + p_0)}{1 + q_0} \right)^{-8/3} - 0.04 \right] \end{aligned} \tag{A54}$$

where $\Gamma(8/3)$ had been replaced by $3/2$. Inserting $J(A)$ into Equation (121) yielded

$$\begin{aligned} \rho^*_{\mathrm{GSL}}(0) \quad &\simeq \quad \frac{B_1 q_0^{1/2} (1 + q_0)^{1/3}}{2^{1/3} \epsilon \phi^{8/3} \cosh^3(X_u)} \left[\left(\frac{4}{3} + \frac{2(k_0 + p_0)}{1 + q_0} \right)^{-8/3} - 0.04 \right] \\ &= \quad \frac{2^{8/3} B_1 q_0^2}{\epsilon (1 + q_0)^{8/3} \phi^{8/3}} \left[\left(\frac{4}{3} + \frac{2(k_0 + p_0)}{1 + q_0} \right)^{-8/3} - 0.04 \right], \end{aligned} \tag{A55}$$

where we used $\cosh^3(X_u) = (1 + q_0)^3/(8q_0^{3/2})$. The approximations (A54) and (A55) are displayed as green dashed lines in Figure 8.

References

1. Schlickeiser, R.; Kröger, M. Compartmental description of the cosmological baryonic matter cycle. I. Competition of triggered star formation, stellar feedback and stellar evolution. *Astron. Astrophys.* **2024**, *692*, A64.

2. Kermack, W.O.; McKendrick, A.G. A contribution to the mathematical theory of epidemics. *Proc. R. Soc. A* **1927**, *115*, 700–721.
3. Kendall, D.G. Deterministic and Stochastic Epidemics in Closed Populations. In Proceedings of the Third Berkeley Symposium on Mathematical Statistics and Probability, Berkeley, CA, USA, 26–31 December 1954; Volume 4, pp. 149–165.
4. Estrada, E. Covid-19 and Sars-Cov-2: Modeling the present, looking at the future. *Phys. Rep.* **2020**, *869*, 1–51.
5. Song, Z.L.; Zhang, Z.; Lyu, F.; et al. From Individual Motivation to Geospatial Epidemiology: A Novel Approach Using Fuzzy Cognitive Maps and Agent-Based Modeling for Large-Scale. *Sustainability* **2024**, *16*, 5036.
6. Li, G.J.; Chang, B.F.; Zhao, J.; et al. VIVIAN: Virtual simulation and visual analysis of epidemic spread data. *J. Visualization* **2024**, *27*, 677–694.
7. Agosto, A.; Cerchiello, P. A data-driven test approach to identify Covid-19 surge phases: An alert-warning tool. *Statistics* **2024**, *58*, 422–436.
8. Yadav, S.K.; Khan, S.A.; Tiwari, M.; et al. Taking cues from machine learning, compartmental and time series models for Sars-Cov-2 omicron infection in Indian provinces. *Spat. Spatio-Temporal Epidemiol.* **2024**, *48*, 100634.
9. Finney, L.; Amundsen, D.E. Asymptotic analysis of periodic solutions of the seasonal SIR model. *Physica D* **2024**, *458*, 133996.
10. Rocha, J.L.; Carvalho, S.; Coimbra, B. Probabilistic Procedures for SIR and SIS Epidemic Dynamics on Erdös-Rényi Contact Networks. *Appliedmath* **2023**, *3*, 828–850.
11. Atienza-Diez, I.; Seoane, L.F. Long- and short-term effects of cross-immunity in epidemic dynamics. *Chaos Solitons Fractals* **2023**, *174*, 113800.
12. Prodanov, D. Computational aspects of the approximate analytic solutions of the SIR model: Applications to modelling of Covid-19 outbreaks. *Nonlinear Dyn.* **2023**, *111*, 15613–15631.
13. Darvishi, H.; Darvishi, M.T. An Analytical Study on Two High-Order Hybrid Methods to Solve Systems of Nonlinear Equations. *J. Math.* **2023**, *2023*, 9917774.
14. Karaji, P.T.; Nyamoradi, N.; Ahmad, B. Stability and bifurcations of an SIR model with a nonlinear incidence rate. *Math. Methods Appl. Sci.* **2023**, *46*, 10850–10866.
15. Chakir, Y. Global approximate solution of SIR epidemic model with constant vaccination strategy. *Chaos Solitons Fractals* **2023**, *169*, 113323.
16. Prodanov, D. Asymptotic analysis of the SIR model and the Gompertz distribution. *J. Comput. Appl. Math.* **2023**, *422*, 114901.
17. Gairat, A.; Shcherbakov, V. Discrete SIR model on a homogeneous tree and its continuous limit. *J. Phys. A* **2022**, *55*, 434004.
18. de Souza, D.B.; Araújo, H.A.; Duarte, G.C.; et al. Fock-space approach to stochastic susceptible-infected-recovered models. *Phys. Rev. E* **2022**, *106*, 014136.
19. Kozyreff, G. Asymptotic solutions of the SIR and SEIR models well above the epidemic threshold. *IMA J. Appl. Math.* **2022**, *87*, 521–536.
20. Tchoumi, S.Y.; Rwezaura, H.; Tchuenche, J.M. Dynamic of a two-strain Covid-19 model with vaccination. *Results Phys.* **2022**, *39*, 105777.
21. Schwarzendahl, F.J.; Grauer, J.; Liebchen, B.; et al. Mutation induced infection waves in diseases like Covid-19. *Sci. Rep.* **2022**, *12*, 9641.
22. Uçar, D.; Çelik, E. Analysis of Covid 19 disease with SIR model and Taylor matrix method. *AIMS Math.* **2022**, *7*, 11188–11200.
23. Hussain, S.; Madi, E.N.; Khan, H.; et al. Investigation of the Stochastic Modeling of Covid-19 with Environmental Noise from the Analytical and Numerical Point of View. *Mathematics* **2021**, *9*, 3122.
24. Lee, K.; Parish, E.J. Parameterized neural ordinary differential equations: Applications to computational physics problems. *Proc. R. Soc. A* **2021**, *477*, 20210162.
25. Bärwolff, G. A Local and Time Resolution of the Covid-19 Propagation-A Two-Dimensional Approach for Germany Including Diffusion Phenomena. *Physics* **2021**, *3*, 536–548.
26. Hynd, R.; Ikpe, D.; Pendleton, T. Two critical times for the SIR model. *J. Math. Anal. Appl.* **2022**, *505*, 125507.
27. Péroux, C.; Howk, J.C. The cosmic baryon and metal cycles. *Annu. Rev. Astron. Astrophys.* **2020**, *58*, 363–406.
28. Tortora, C.; Hunt, L.K.; Ginolfi, M. Scaling relations and baryonic cycling in local star-forming galaxies I. The sample. *Astron. Astrophys.* **2022**, *657*, A19.
29. Mercado, F.J.; Bullock, J.S.; Boylan-Kolchin, M.; et al. A relationship between stellar metallicity gradients and galaxy age in dwarf galaxies. *Mon. Not. R. Astron. Soc.* **2021**, *501*, 5121–5134.
30. Kröger, M.; Schlickeiser, R. Verification of the accuracy of the SIR model in forecasting based on the improved SIR model with a constant ratio of recovery to infection rate by comparing with monitored second wave data. *R. Soc. Open Sci.* **2021**, *8*, 211379.
31. Tumlinson, J.; Peeples, M.S.; Werk, J.K. The circumgalactic medium. *Annu. Rev. Astron. Astrophys.* **2017**, *55*, 389–432.
32. Pandya, V.; Fielding, D.B.; Bryan, G.L.; et al. A Unified Model for the Coevolution of Galaxies and Their Circumgalactic Medium: The Relative Roles of Turbulence and Atomic Cooling Physics. *Astrophys. J.* **2023**, *956*, 118.

33. Haas, F.; Kröger, M.; Schlickeiser, R. Multi-Hamiltonian structure of the epidemics model accounting for vaccinations and a suitable test for the accuracy of its numerical solvers. *J. Phys. A* **2022**, *55*, 225206.
34. Weisstein, E. *The CRC Encyclopedia of Mathematics*, 3rd ed.; Chapman and Hall/CRC Press: Boca Raton, FL, USA, 2009.
35. Beyer, W.H. *CRC Standard Mathematical Tables*, 28th ed.; CRC Press: Boca Raton, FL, USA, 1987; p. 455.
36. Shampine, L.F.; Reichelt, M.W. The MATLAB ODE suite. *SIAM J. Sci. Comput.* **1997**, *18*, 1–22.
37. Abramowitz, M.; Stegun, I.A. *Handbook of Mathematical Functions with Formulas, Graphs, and Mathematical Tables*; Dover Publications: New York, NY, USA, 1972.
38. Madau, P.; Dickinson, M. Cosmic star formation history. *Annu. Rev. Astron. Astrophys.* **2014**, *52*, 415–486.
39. Madau, P.; Fragos, T. Radiation backgrounds at cosmic dawn: X-rays from compact binaries. *Astrophys. J.* **2017**, *840*, 39.
40. Labbé, I.; van Dokkum, P.; Nelson, E.; et al. A population of red candidate massive galaxies 600 Myr after the Big Bang. *Nature* **2023**, *616*, 266–269.
41. Dahlen, T.; Mobasher, B.; Dickinson, M.; et al. Evolution of the luminosity function, star formation rate, morphology, and size of star-forming galaxies selected at rest-frame 1500 and 2800 Angstrom. *Astrophys. J.* **2007**, *654*, 172–185.
42. Cucciati, O.; Tresse, L.; Ilbert, O.; et al. The star formation rate density and dust attenuation evolution over 12 Gyr with the VVDS surveys. *Astron. Astrophys.* **2012**, *539*, A31.
43. Perez-Gonzalez, P.G.; Rieke, G.H.; Villar, V.; et al. The stellar mass assembly of galaxies from $z = 0$ to $z = 4$: Analysis of a sample selected in the rest-frame near-infrared with spitzer. *Astrophys. J.* **2008**, *675*, 234–261.
44. Moustakas, J.; Coil, A.L.; Aird, J.; et al. PRIMUS: Constraints on star formation quenching and galaxy merging, and the evolution of the stellar mass function from $z = 0$–1. *Astrophys. J.* **2013**, *767*, 50.
45. Bland-Hawthorn, J.; Gerhard, O. The galaxy in context: Structural, kinematic, and integrated properties. *Annu. Rev. Astron. Astrophys.* **2016**, *54*, 529–596.
46. Catinella, B.; Saintonge, A.; Janowiecki, S.; et al. xGASS: Total cold gas scaling relations and molecular-to-atomic gas ratios of galaxies in the local Universe. *Mon. Not. R. Astron. Soc.* **2018**, *476*, 875–895.
47. Calette, A.R.; Avila-Reese, V.; Rodríguez-Puebla, A.; et al. The HI- and H2-to-Stellar Mass Correlations of Late- and Early-Type Galaxies and their Consistency with the Observational Mass Functions. *Rev. Mex. Astron. Astrofis.* **2018**, *54*, 443–483.
48. Kroupa, P. On the variation of the initial mass function. *Mon. Not. R. Astron. Soc.* **2001**, *322*, 231–246.
49. Chabrier, G. Galactic stellar and substellar initial mass function. *Publ. Astron. Soc. Pac.* **2003**, *115*, 763–795.
50. Conroy, C. Modeling the panchromatic spectral energy distributions of galaxies. *Annu. Rev. Astron. Astrophys.* **2013**, *51*, 393–455.